OAK RIDGE NATIONAL LABORATORY LIBRARIES
3 4456 0550252 3

CENTRAL RESEARCH LIBRARY

ORNL-TM-4530

Cy 73

CALCULATIONS RELATED TO THE APPLICATION OF SILICON DETECTORS IN PION RADIOBIOLOGY

Tony W. Armstrong
Kay C. Chandler

OAK RIDGE NATIONAL LABORATORY
CENTRAL RESEARCH LIBRARY
DOCUMENT COLLECTION
LIBRARY LOAN COPY
DO NOT TRANSFER TO ANOTHER PERSON
If you wish someone else to see this document, send in name with document and the library will arrange a loan.
UCN-7969
(3 3-67)

OAK RIDGE NATIONAL LABORATORY
OPERATED BY UNION CARBIDE CORPORATION • FOR THE U.S. ATOMIC ENERGY COMMISSION

This report was prepared as an account of work sponsored by the United States Government. Neither the United States nor the United States Atomic Energy Commission, nor any of their employees, nor any of their contractors, subcontractors, or their employees, makes any warranty, express or implied, or assumes any legal liability or responsibility for the accuracy, completeness or usefulness of any information, apparatus, product or process disclosed, or represents that its use would not infringe privately owned rights.

ORNL-TM-4530

Contract No. W-7405-eng-26

Neutron Physics Division

CALCULATIONS RELATED TO THE APPLICATION OF SILICON DETECTORS IN PION RADIOBIOLOGY*

Tony W. Armstrong
Kay C. Chandler†

Note:

This work was funded
by the
NATIONAL SCIENCE FOUNDATION
under Order NSF/RANN AG-399

MAY 1974

*Submitted for journal publication.

†Computer Sciences Division.

NOTICE This document contains information of a preliminary nature and was prepared primarily for internal use at the Oak Ridge National Laboratory. It is subject to revision or correction and therefore does not represent a final report.

OAK RIDGE NATIONAL LABORATORY
Oak Ridge, Tennessee, 37830
operated by
UNION CARBIDE CORPORATION
for the
U. S. ATOMIC ENERGY COMMISSION

OAK RIDGE NATIONAL LABORATORY LIBRARIES

3 4456 0550252 3

TABLE OF CONTENTS

	Page
ABSTRACT	1
ACKNOWLEDGMENT	2
1. INTRODUCTION	3
2. METHOD OF CALCULATION	6
3. RESULTS	10
3.1 Products from π^- Capture	10
3.2 Pulse-Height Spectra	12
3.3 Integral Energy Deposition	21
3.4 Total Energy Deposition	23
3.5 Energy Deposition Spectra	27
3.6 Inferring Tissue Energy Deposition From Detector Response	32
APPENDIX A	42
APPENDIX B	54
APPENDIX C	56
APPENDIX D	63
REFERENCES	65

CALCULATIONS RELATED TO THE APPLICATION OF SILICON DETECTORS IN PION RADIOBIOLOGY*

Tony W. Armstrong
Kay C. Chandler

Oak Ridge National Laboratory
Oak Ridge, Tennessee, 37830

Abstract

Calculations have been made of the pulse-height spectrum and energy deposition in silicon detectors of various thicknesses (10, 50, 300, 1000, and 3000 microns) placed in a large region of π^--mesons stopping in tissue. The contribution of π^- captures within the detectors is determined, and the energy deposition in the detector is compared to the actual energy deposition in the tissue with the detector removed. A method for inferring the energy deposition in the tissue by various types of particles from the pulse-height spectra of the thin detectors is discussed and evaluated.

*This research was funded by the National Science Foundation, Order NSF/RANN AG-399, under Union Carbide Corporation's contract with the U. S. Atomic Energy Commission.

ACKNOWLEDGMENT

This work from its beginning has been carried out in close collaboration with Dr. C. Richman of the Los Alamos Scientific Laboratory, whose interest and guidance have been invaluable.

1. INTRODUCTION

The radiation field in the vicinity of a stopping negatively charged pion beam is rather complex because of the numerous types of charged and uncharged particles that are produced when a negatively charged pion is captured by a nucleus and because of the wide energy range over which the particles are produced. Since biological effect is dependent upon particle type and energy, it is important in pion radiobiology directed toward radiotherapy to have means of measuring not only the spatial distribution of the total absorbed dose produced by π^- beams in tissue-equivalent phantoms but also the contributions to the absorbed dose by various types of particles.

Silicon semiconductor detectors have certain inherent characteristics (e.g., linearity, fast response, small size) which make them attractive dosimetric devices for pion radiobiology[1,2]. However, silicon detectors are not tissue-equivalent. Mass stopping powers for tissue-like materials and silicon are substantially different, and according to theoretical predictions[3], the charged-particle energy production from π^- captures in silicon is $\approx$ 25% less than in tissue.

The response of a silicon detector located in the stopping region of a pion beam is expected to be dependent upon the size of the detector. For thin ($\sim$ tens of microns) detectors, the energy deposition in the detector will be due primarily to those particles passing through the detector that have been produced outside the detector, whereas for thick ($\sim$ several millimeters) detectors, the response will be influenced by π^- captures taking place inside the detector. To relate the measured energy deposition in thin silicon detectors to the actual energy deposition in tissue-equivalent material involves only stopping-power and density corrections, whereas for

thick detectors, differences in π^- capture products must also be considered. Another potential advantage of thin detectors is the possibility of inferring from the measured pulse-height spectrum the contribution to the tissue-equivalent absorbed dose due to different types of particles. Thus in pion radiobiology, thick silicon detectors for practical reasons[2]) may be advantageous in mapping the relative dose distributions and in determining the spatial distribution of stopping pions, whereas in the stopping region thin silicon detectors may be better suited for estimating the tissue-equivalent dose and the contributions to the dose by various capture products.

In the present work, the response of silicon detectors of various thicknesses (10, 50, 300, 1000, and 3000 microns) to stopping pions is investigated by means of calculations. The detector is assumed to be located in the middle of a large π^- stopping region in tissue. The products from the π^- captures in the tissue and in the silicon are determined using a theoretical nuclear model[4]), which has been shown to give results for light nuclei in approximate agreement with measurements[5]). A Monte Carlo calculation is performed for each capture and the energy deposition in the silicon by each charged-particle product is determined using computed stopping powers and ranges. Thus, fluctuations in the particle production and correlations caused by more than one particle per capture contributing to the energy deposition are properly taken into account so that the analog of a measured pulse-height spectrum (PHS) is obtained.

The energy deposition in the tissue with the silicon removed has also been computed. By knowing both the silicon and tissue doses, methods for inferring the tissue dose from the silicon PHS can be evaluated. Such methods are not fully investigated here, but one rather straightforward, although approximate, method is discussed.

Several simplifying assumptions have been made in carrying out these initial calculations. For example, only a one-dimensional configuration is considered; i.e., both the capture region and the detector are taken to be infinite in radius. Also, the contribution of neutrons and photons to the energy deposition, which is expected to be small in the middle of the capture region where the detector is placed, is not included. While these simplifications should not have a major effect on the main purposes here of determining the general influence of detector thickness on the PHS and in determining the contributions of individual particle types to the PHS, they should be kept in mind in interpreting the results. Also, it should be noted that the results here are somewhat restrictive because the PHS is expected to be influenced by the spatial distribution of the π^- captures, and only a single capture distribution has been considered in all of the calculations here.

In the next section the details of the calculational method are described and in the last section the results are presented and discussed.

2. METHOD OF CALCULATION

The case of interest is that of a small piece of silicon (say, 10 μ to 3 mm thick, 2 to 5 mm in radius) located in a large region of stopping negatively charged pions in a tissue-equivalent material (fig. 1). In all of the calculations here, a one-dimensional approximation (fig. 1) has been used with the detector placed at the midpoint of a region 5 cm in width containing a uniform density of π^- captures. The material on either side of the detector was taken to have an approximate tissue composition with the following atom concentrations (in percent): H, 63.3; O, 25.8; C, 9.5; N, 1.4.

The energy deposition in the detector was computed using Monte Carlo methods. First, the position of a π^- capture was selected assuming a uniform spatial distribution of captures within the 5-cm interval. If the capture is in the tissue, the type of nucleus (C, N, or O) capturing the pion is determined using the Fermi-Teller Z-law[6]) for the capture probabilities. A Monte Carlo calculation using subroutine versions[3]) of Bertini's intranuclear-cascade program[4]) and Guthrie's evaporation program[7]) is then made to obtain the particle type and energy of each of the capture products. Similarly, if the capture takes place inside the detector, an intranuclear-cascade-evaporation calculation is performed for a π^- capture by a silicon nucleus. For each charged-particle product (proton, deuteron, triton, ^{3}He, alpha particle, or residual nucleus), the contribution to the energy deposition in the detector is determined assuming isotropic emission and using computed ranges and stopping powers (see fig. 2). It is important to note that by computing the products from each capture separately and by determining the energy deposition from each product separately, correlations resulting

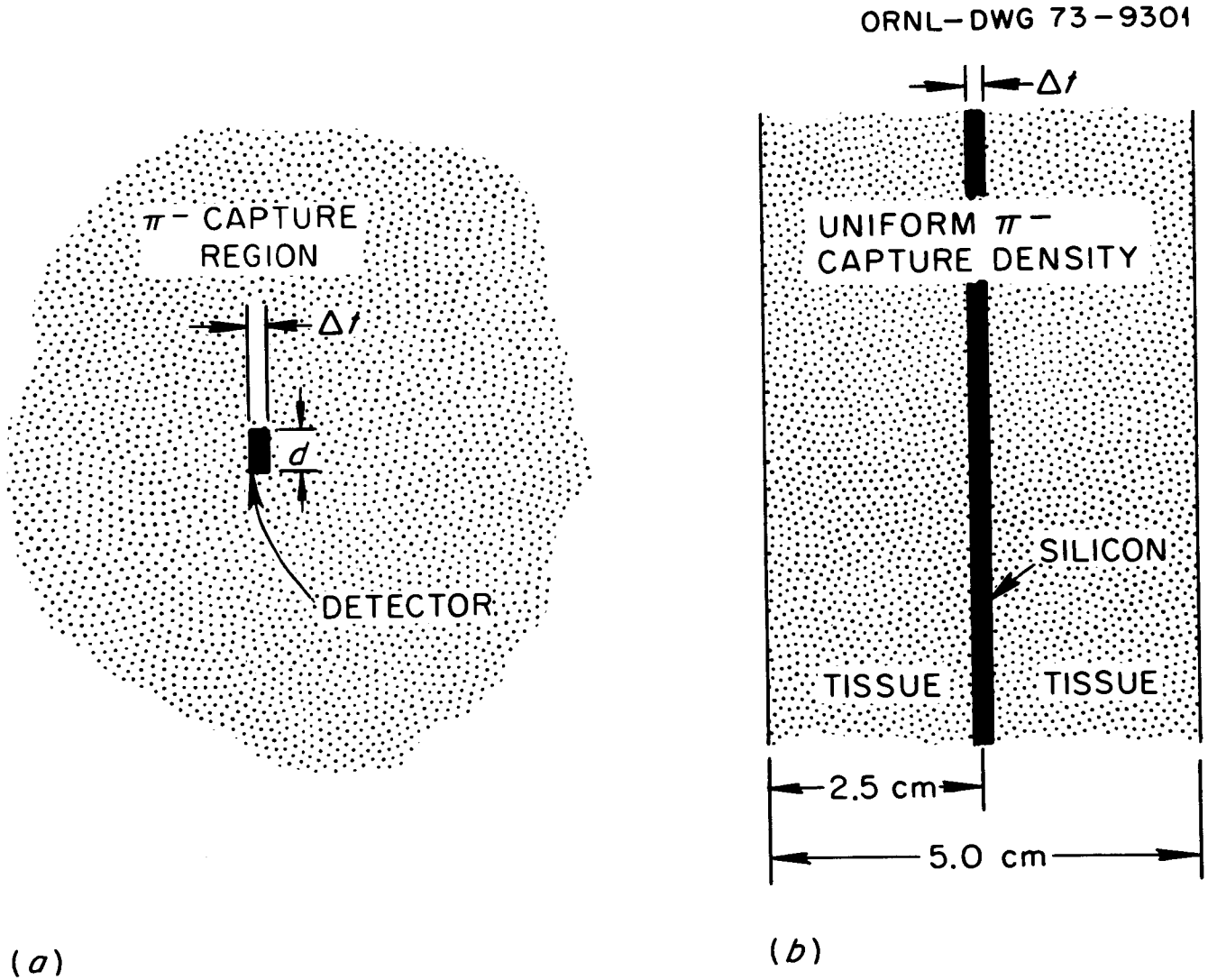

Fig. 1. Configuration of interest (a) and one-dimensional approximation used in the calculations (b).

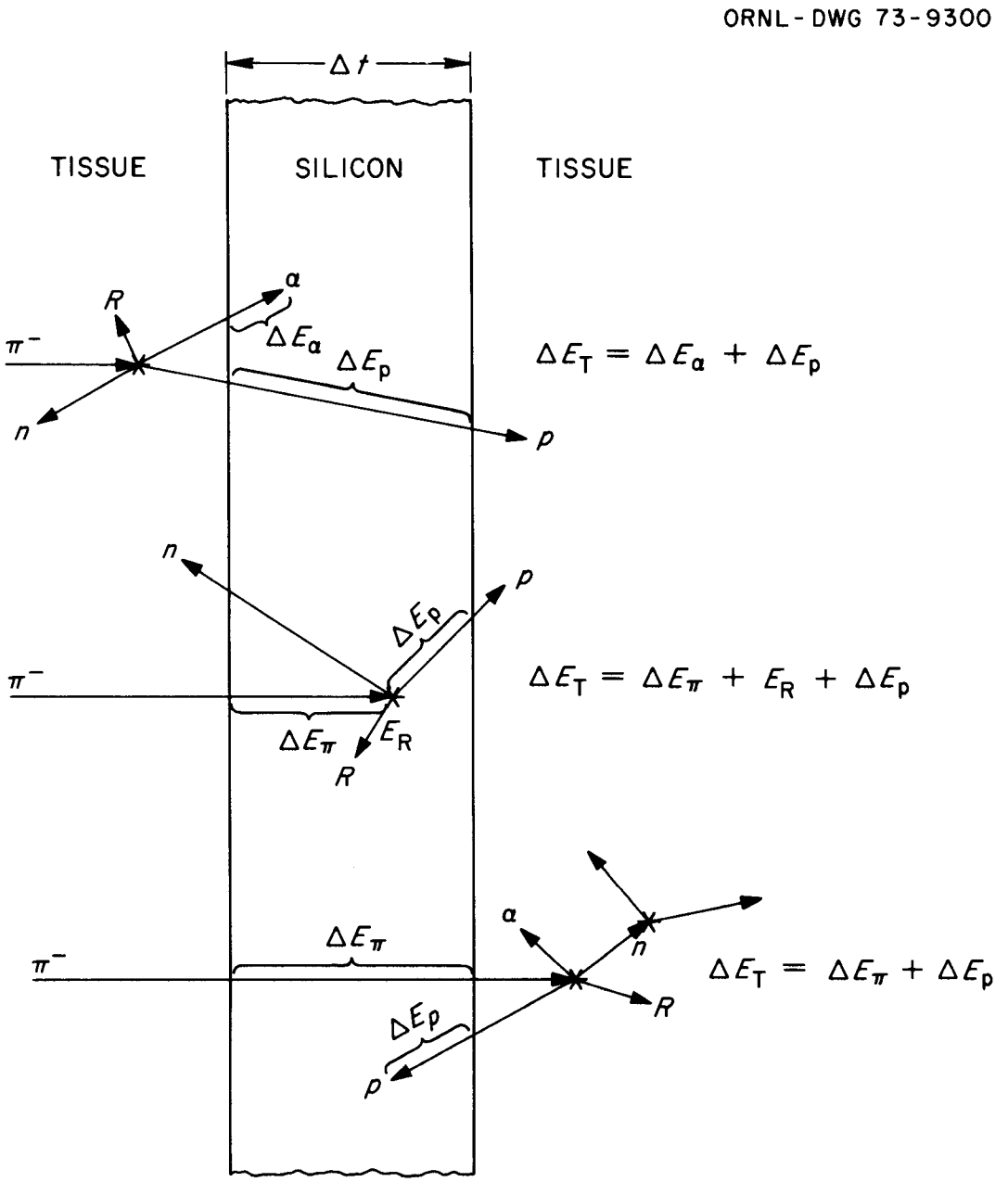

Fig. 2. Illustration of several cases in computing the energy deposition in the detector. ΔE_T is the energy deposition for the capture.

from more than one particle per capture contributing to the energy deposition are taken into account properly.

It is assumed that the captures result from the slowing down of a parallel beam of pions incident on the left side of the detector. Thus, for each capture occurring inside the detector or in the tissue on the right side of the detector, a contribution to the energy deposition for this capture by the ionization produced by the slowing-down pion is also included (see fig. 2).*

The energy deposition by neutrons and photons from π^- capture and by secondary nuclear interactions produced by the π^- capture products is not included, which simplifies the calculations substantially. For the particular configuration considered where the detector is in the middle of a large capture region, these contributions are expected to be small.

Stopping powers and ranges were computed as needed by using a subroutine version of the SPAR code[8].† Normally, the energy of the particles entering or leaving the detector and the energy deposition within the detector were computed using residual ranges. For example, for a particle entering the detector with energy E_o and traveling a distance $\Delta\ell$ through the detector, the energy deposition was computed as E_o minus the energy corresponding to a residual range in silicon of $R(E_o) - \Delta\ell$. For very large values of $R(E_o)/\Delta\ell$, this procedure is subject to error because of numerical roundoff. Therefore, the criterion was used that for $R(E_o)/\Delta\ell > 500$, the energy deposition was computed using the stopping power - i.e., $\Delta E = S(E_o)\ \Delta\ell$.

*It is assumed that in practical applications the detector system will be capable of identifying the response due to the beam contaminants, and therefore the contributions of incident electrons and muons passing through the detector are not considered in the calculations.

†Stopping powers and ranges for various particles in tissue and in silicon are given in Appendix A.

3. RESULTS

3.1 Products from π^- Capture

The multiplicities and energy spectra of the products (neutrons, protons, deuterons, tritons, ^{3}He's, alpha particles, and residual nuclei) from π^- capture in tissue and in silicon as computed using the intranuclear-cascade-evaporation model have already been published[3]). Table 1 gives a summary of the results presented in ref. 3 for tissue and silicon. In this table and throughout the paper, alpha particles, ^{3}He's, tritons, and deuterons are grouped as "heavy particles." Also, all residual nuclei (stable and radioactive) are grouped as "recoils" with the exception that ^{8}Be is assumed to decay immediately into two alpha particles, and these alpha particles are included under "heavy particles." These groupings are made just to simplify the presentation of the results. In determining the energy deposition, the particle production and the stopping powers and ranges for each individual particle type were computed.

Note from Table 1 that the main difference in the particle production from captures in silicon and in tissue is in the number and energy of the heavy-particle production. The detailed results given in ref. 3 show that this is mainly due to a difference in alpha-particle production. There is approximately one-third as many alpha particles produced per capture in silicon as compared to tissue, and the energy carried away by alpha particles is almost a factor of five less for silicon. The total kinetic energy of all of the charged particles produced is about 25% less for silicon (30.1 vs 38.1 MeV per capture).

TABLE 1

Charged-Particle Multiplicities and Energies From π^- Captures in Tissue and in Silicon

Particle Type	Number Per π^- Capture		Kinetic Energy Per Capture (MeV)	
	Tissue	Silicon	Tissue	Silicon
Protons	1.20	1.82	19.6	22.1
Heavy Particles	1.59	0.73	17.0	5.71
Recoils	0.49	0.99	1.54	2.25
Total Charged-Particle Energy Release:			38.1	30.1

3.2 Pulse-Height Spectra

Figure 3 shows the computed pulse-height spectrum for a silicon detector 50 μ in thickness. The PHS is computed as

$$N_i = \frac{n_i}{\Delta E_i \ \rho \ \Delta t \ N_c} \ ,$$

where

n_i = the number of captures, out of a total number of N_c captures that take place in the entire capture volume, which produce an energy deposition in the silicon that falls within the energy interval from E_i to $E_i + \Delta E_i$,

ΔE_i = the width in MeV of the energy interval,

ρ = the density of silicon (= 2.33 g cm^{-3}), and

Δt = the detector thickness in cm.

N_i [or N(E), the continuous-variable representation of N_i used in the labeling of the ordinate in fig. 3] will be referred to as the "total correlated" PHS; that is, in computing N_i the sum of the energy depositions from all particles coming from the same capture is used in determining the energy interval in which the capture contributes. Thus, correlations in the energy deposition which occur when more than one particle from the same capture deposit energy in the detector are included in the computation of N_i, so that N_i is analogous to the PHS that would be measured. The units for N_i[N(E)] are written in fig. 3 as "events/(capture MeV g cm^{-2})," where "events" refer to captures that make a contribution to the energy deposition in the detector and "capture" refers to the total number of captures that take place, N_c. Dividing the energy deposition by N_c is somewhat arbitrary, and some other choices of normalization would have served as well.

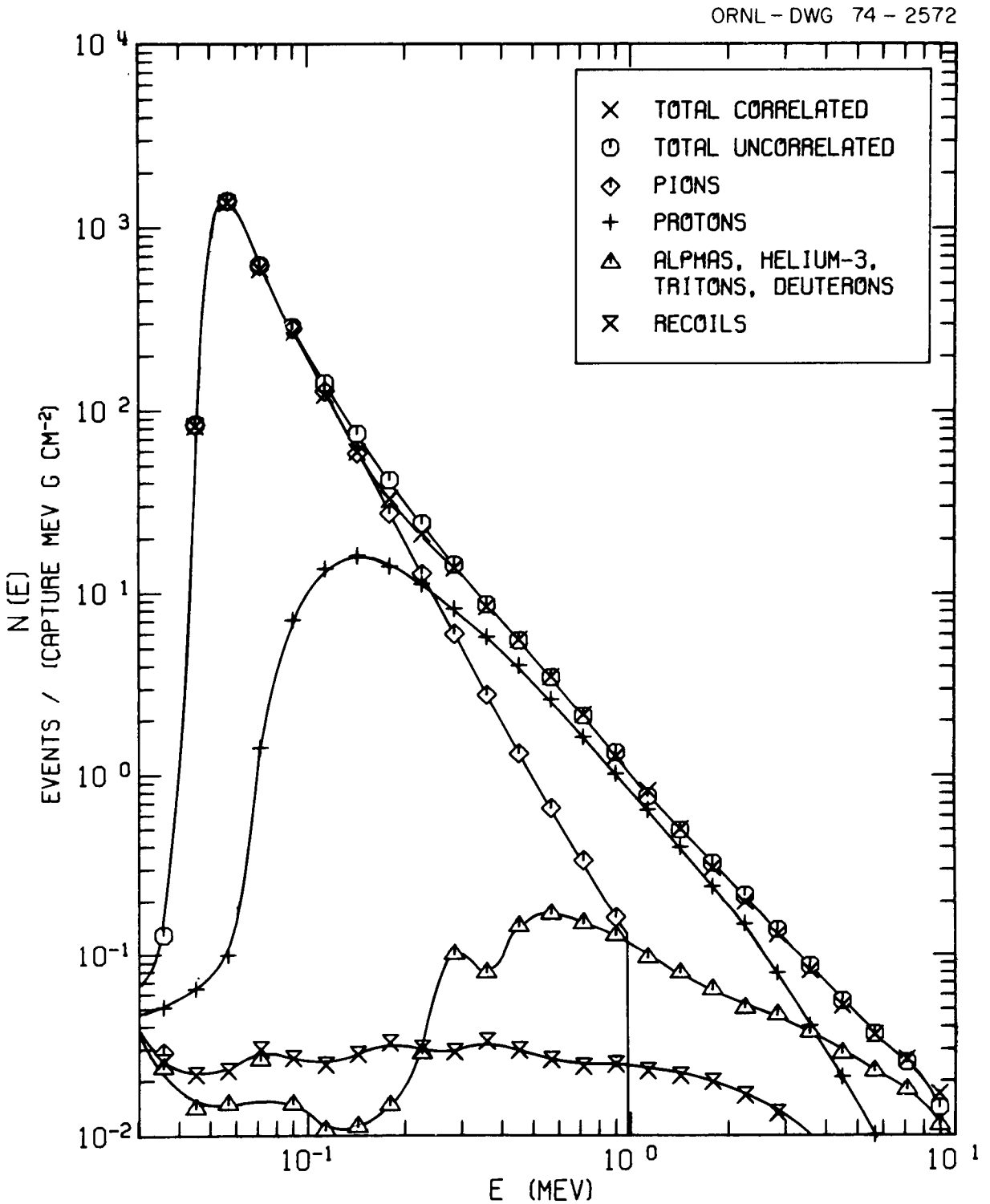

Fig. 3. Pulse-height spectra for silicon detector 50 μ in thickness.

Figure 3 also shows the pulse-height spectrum due to various particle types and the "total uncorrelated" spectrum. Letting N'_{ij} denote the spectrum due to the jth particle type (pions, protons, heavy particles, and recoils), the total uncorrelated spectrum is computed as

$$N'_i = \sum_j N'_{ij} \ .$$

In computing the spectrum for various particle types, N'_{ij}, the energy deposition by particles of different types are considered separately in determining the energy interval in which the contribution occurs. For example, if protons from a capture deposit energy E_p in the detector and alpha particles from the same capture deposit E_α, then this capture contributes to the proton spectrum in the energy interval containing E_p and to the heavy-particle spectrum in the interval containing E_α. (The contribution to the total correlated spectrum in this case would be in the energy interval in which $E_p + E_\alpha$ falls.) The total uncorrelated spectrum, N'_i, for a given energy interval is simply the sum of the contributions of all particle types for this interval and does not, in general, correspond to the spectrum that would be measured. The reason for computing the uncorrelated spectrum is, as subsequent results will show, for thin detectors ($\leqslant 50\ \mu$) there is little difference in the correlated and uncorrelated spectra, and in these cases the uncorrelated spectra are helpful in identifying the contribution to the total spectrum made by particular types of particles.

The large pion contribution shown in fig. 3 is due to those pions passing through the detector and stopping on the other side. For the configuration chosen, the maximum range of a pion incident on the detector is about 2.5 cm in tissue, which corresponds to a kinetic energy of about 23 MeV.

Pions at 23 MeV deposit 0.05 MeV in passing through 50 μ of silicon, and these pions produce the maximum in the pion curve shown in fig. 3. Pions stopping closer to the detector have lower energies, higher stopping powers, and produce larger energy depositions in passing through the detector. The pion contribution stops at a maximum energy deposition of about 1 MeV, corresponding to the energy of a pion having a range of 50 μ in silicon (see Table 2). Thus, the pion curve is particularly dependent upon the spatial distribution of the captures and upon the position of the detector in the capture region.

The peak in the proton curve in fig. 3 occurs at an energy deposition of $E \approx 0.15$ MeV and corresponds to high-energy ($\gtrsim$ 35 MeV) protons passing through the detector. For $E \lesssim 0.15$ MeV, the proton curve decreases because of the decreasing number of protons which are produced at high energies and which reach the detector at high energies. For $E \gtrsim 0.15$ MeV, the proton spectrum is due to lower ($\lesssim$ 35 MeV) energy protons with higher stopping powers producing larger energy depositions. There is a change in slope of the proton curve at $E \approx 2$ MeV, which is the energy corresponding to a proton range of 50 μ in silicon.

Figure 3 shows that for a 50-μ detector there is little difference between the correlated and uncorrelated spectra. This does not mean that correlations do not occur, but that the effect of correlations is small. For example, if a capture takes place to the right of the detector and a proton from the capture deposits energy E_p in the detector, the energy deposition by the proton is in correlation with the energy E_π deposited by the pion passing through the detector. For thin detectors, however, E_π is relatively small so that E_p is not much different from $E_p + E_\pi$.

TABLE 2

Energy (MeV) Corresponding to a Residual Range of Δt (microns) in Silicon

Δt	Particle Type			
	Pions	Protons	Alpha Particles	Neon Ions[a]
10	0.36	0.69	2.2	18.2
50	0.95	2.0	7.7	82.7
300	2.7	6.0	23.8	
1000	5.3	12.1	48.3	
3000	9.8	22.6	90.2	

a. The calculations in ref. 3 show that the average charge number of the residual nuclei following π^- capture in silicon is Z = 10.

As an example of the response of a thick detector, fig. 4 shows the PHS for $\Delta t = 1000\ \mu$. Compared to the 50-μ case, the contributions of all particle types except recoils are shifted to higher energy depositions because of the larger thickness of silicon traversed. For both 50 μ and 1000 μ, the recoil contribution is mainly from captures within the silicon, and therefore the recoil spectrum is about the same for both thicknesses.* The change in the relative contribution of various particle types with detector thickness will be discussed in more detail later. Note from fig. 4 that there is a substantial difference between the correlated and uncorrelated spectra.**

The total correlated spectra for different silicon thicknesses are compared in fig. 5. To indicate the nonlinearity with respect to detector thickness, these spectra are plotted as a function of E^*, where E^* is the energy deposition (in MeV) divided by the detector thickness (in g cm^{-2}). When E^* is used as the independent variable, the pion peak occurs at the same value of E^* for all thicknesses because the average mass stopping power of the pions passing through the detector is approximately the same. When presented as in fig. 5, the spectra for various thicknesses appear similar, although it is apparent that over the whole range of thicknesses there are effects at values of E^* outside the pion peak that are nonlinear with

*In interpreting some of the results, it is helpful to know the energy deposited by the capture products as a function of the distance from the capture site. This information has been computed for silicon and for tissue and is given in Appendix B.

**Spectra like those shown in figs. 3 and 4 for the other thicknesses considered and the effect of captures within the detector on the PHS are given in Appendix C.

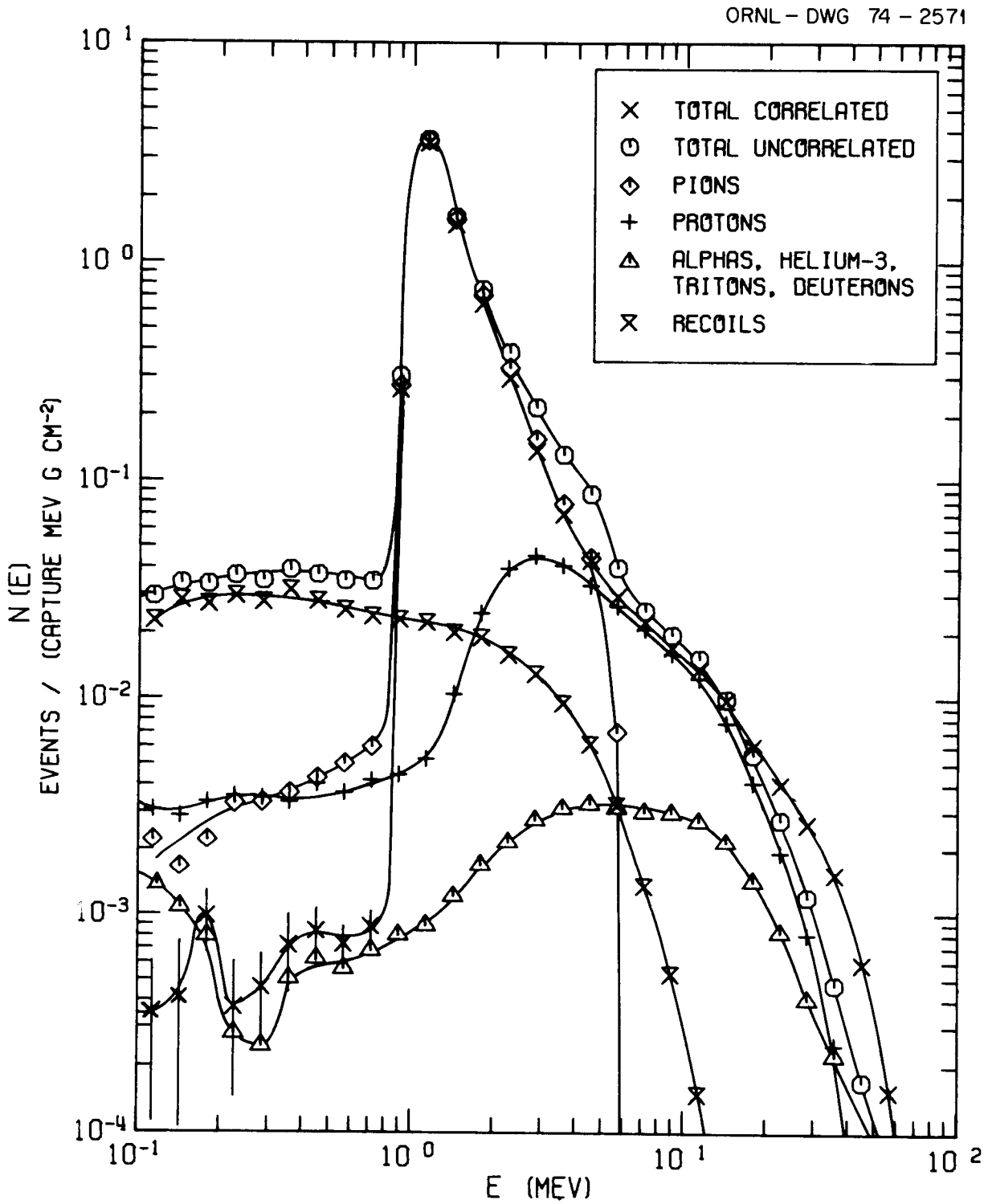

Fig. 4. Pulse-height spectra for silicon detector 1000 μ in thickness. Error bars (one standard deviation) are shown for the total correlated spectra, but they are appreciable only at the very low energies.

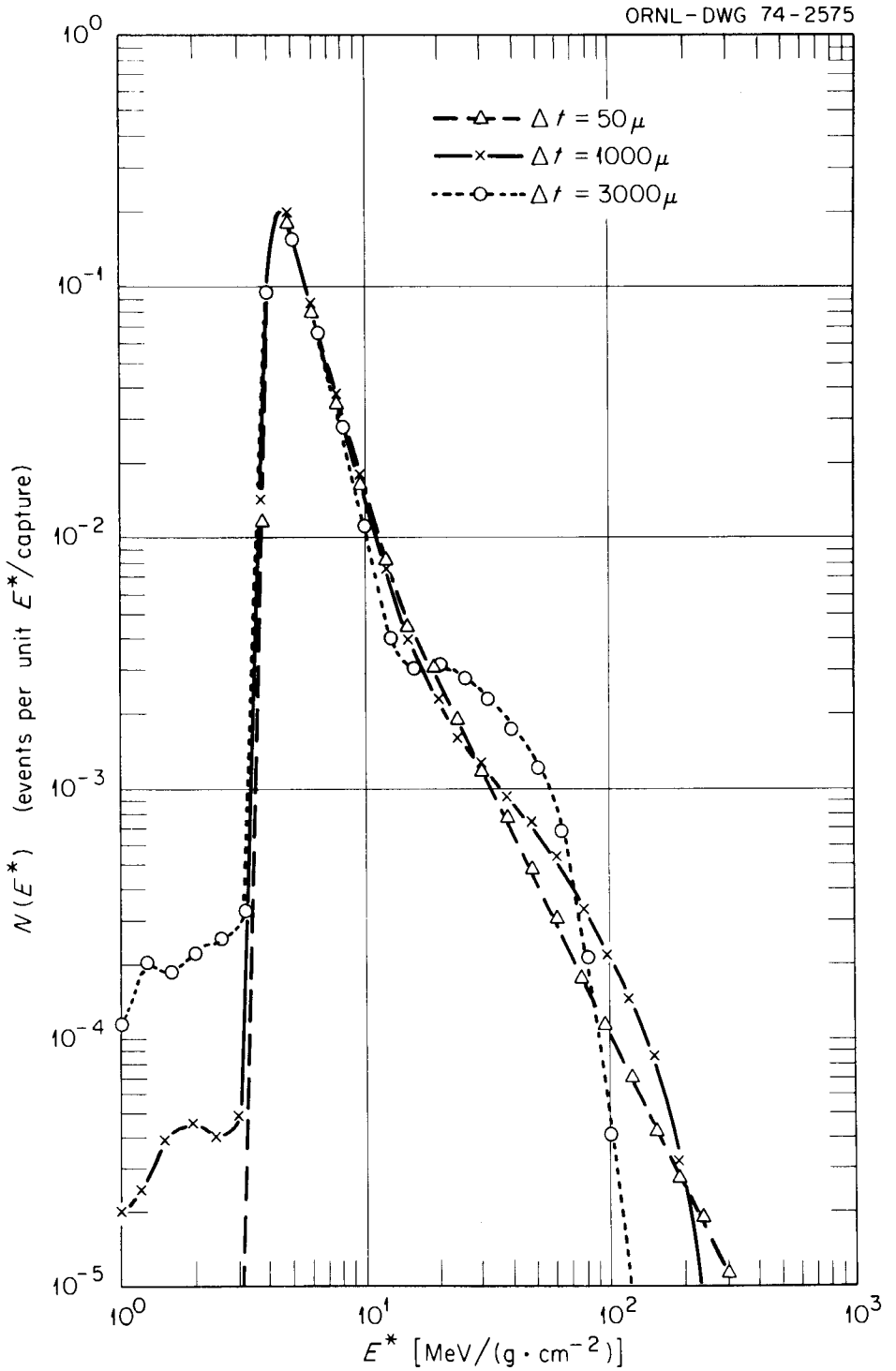

Fig. 5. Total correlated spectra for detectors of various thicknesses as a function of E^*, the energy deposited (in MeV) per unit detector thickness (in g cm^{-2}).

thickness. As will be shown later, the pulse-height data can be presented in a different way which will make more apparent the differences in the high-energy portions of the spectra.

3.3 Integral Energy Deposition

An important practical consideration in the application of silicon detectors is the energy range over which the energy depositions or pulses take place (e.g., ref. 2). This is because system linearity must be maintained over an energy range sufficiently large to include energy depositions that represent practically all of the energy deposited in the detector.

The low end of the energy range is defined by the energy loss due to pions (and in some situations, muons and electrons) passing through the detector and can be estimated from the energy of the incident beam, the stopping power of silicon, and the thickness of the detector. A practical high-energy limit can be determined from the PHS. Figure 6 shows f(E), the fraction of the total energy deposited in the detector by events depositing energy > E, where

$$f(E) = \frac{\int_E^\infty N(E')E'dE'}{\int_0^\infty N(E')E'dE'}$$

and N is the total correlated PHS. For example, fig. 6 shows that in the capture region 99% of the energy deposited in a 50-μ detector is by pulses $\leqslant$ 25 MeV. Figure 6 also shows the distribution measured by Raju *et al.*[2]) using a silicon detector 2-mm thick and 5 mm in radius located in a π^- capture region. Although the calculated and measured distributions are for different detector sizes, beams, and capture volumes, there is good qualitative agreement.

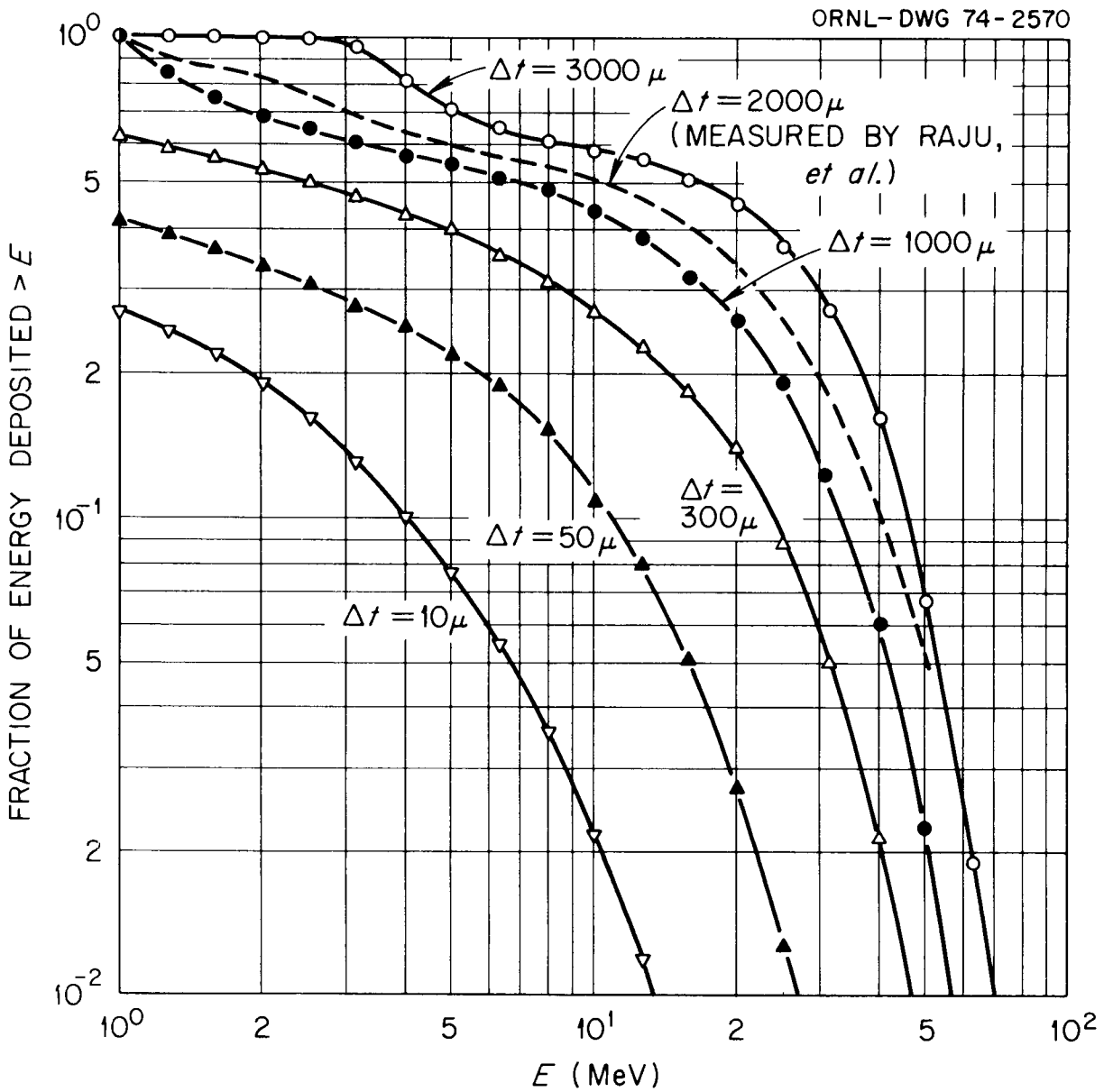

Fig. 6. The fraction of the total energy deposition in detectors of various thicknesses due to events producing an energy deposition > E. The measured distribution (ref. 2) was obtained using a detector 2-mm thick and 5 mm in radius.

3.4 Total Energy Deposition

Table 3 shows the energy deposition for various thicknesses of silicon and tissue. In terms of the PHS, the energy deposition for the jth particle-type category is

$$\varepsilon_j = \sum_i N'_{ij} \bar{E}_i \Delta E_i ,$$

and the total energy deposition for all particle types is

$$\varepsilon = \sum_j \varepsilon_j$$

or

$$\varepsilon = \sum_i N_i \bar{E}_i \Delta E_i ;$$

that is, the total energy deposition is the same whether computed from the correlated or the uncorrelated pulse-height spectrum.

Table 3 also gives the contribution to the energy deposition in silicon due only to captures that take place within the silicon. For the thin detectors (10 and 50 μ), almost all of the energy is deposited by particles from captures in tissue except for the case of recoils. However, the contribution of recoils is very small, so the total energy deposition is affected little by the captures within the silicon. Calculations have also been made (see Appendix D) which show that the differences in the energy depositions for tissue and silicon for Δt = 10 and 50 μ are, except for recoils, due to differences in stopping powers and ranges and not to differences in tissue and silicon capture products. Thus, these thin detectors act as probes in the sense that their response is due almost entirely to the π^- capture particles produced outside, rather than within, the detector.

TABLE 3

Energy Deposition in Silicon and in Tissue[a,b]

Particle Type	Silicon[c]				
	Δt = 10 μ	Δt = 50 μ	Δt = 300 μ	Δt = 1000 μ	Δt = 3000 μ
Pions	3.63 (0.5)	3.62 (1.4)	3.55 (4.1)	3.46 (8.4)	3.33 (16)
Protons	2.76 (1.9)	2.75 (6.3)	2.77 (19)	2.69 (32)	2.47 (47)
Heavy Particles	2.04 (4.2)	1.65 (12.7)	1.07 (34)	0.74 (59)	0.58 (82)
Recoils	0.24 (75)	0.21 (91)	0.20 (98)	0.19 (100)	0.19 (100)
Total	8.7 (3.9)	8.2 (7.6)	7.6 (16)	7.1 (25)	6.6 (36)

Particle Type	Tissue				
	Δt = 10 μ	Δt = 50 μ	Δt = 300 μ	Δt = 1000 μ	Δt = 3000 μ
Pions	4.63	4.64	4.63	4.63	4.64
Protons	3.74	3.70	3.73	3.74	3.69
Heavy Particles	3.37	3.32	3.37	3.38	3.36
Recoils	0.34	0.34	0.34	0.34	0.34
Total	12.1	12.0	12.1	12.1	12.0

a. Statistical errors (one standard deviation) of all values in the table are generally less than 2%.

b. Energy deposition values in units of MeV per unit thickness in g cm^{-2} per π^- capture.

c. Values in parentheses are the contributions (in percent) to the energy deposition by captures taking place in the silicon.

The energy deposition in tissue shown in Table 3 was computed for the same Δt intervals and at the same positions within the capture region as for the silicon. Since even the largest thickness considered is much smaller than the width of the capture region, the energy depositions in tissue are the same (within statistics) for all Δt.

The energy deposition in tissue computed here can be compared with the dose computed previously[10]) for a π^- beam incident on a tissue phantom. There a detailed transport calculation was made using the code[11]) HETC in which the contributions from neutrons and photons from π^- capture, all secondary nuclear interactions, muons from π^- decay, etc. were included. In ref. 10 the energy distribution of the incident beam was chosen to produce a uniform π^--capture distribution over the depth interval from 12.5 to 17.5 cm in the tissue phantom, so the size of the capture region was the same as that considered here. From the previous calculations[10]), the laterally integrated absorbed dose at a depth of 15.0 cm (the midpoint of the capture region) is 1.83×10^{-7} rad cm^{-2} (incident pion)$^{-1}$. In the previous calculations, it was also found that for this beam approximately 85% of the incident pions undergo π^- capture rather than decay or nuclear interaction in flight. From the energy deposition for tissue given in Table 3, the dose per incident pion is

$$D = \left[12.1 \frac{\text{MeV}}{\text{g cm}^{-2}\ \text{capture}}\right] \left[0.85 \frac{\text{capture}}{\text{incident pion}}\right] \times \left[1.6 \times 10^{-6} \frac{\text{erg}}{\text{MeV}}\right] \left[10^{-2} \frac{\text{rad}}{\text{erg g}^{-1}}\right]$$

$$= 1.65 \times 10^{-7} \text{ rad cm}^2/\text{incident pion} .$$

Thus the approximate calculations here give a dose within about 10% of the more detailed transport calculations, and therefore the simplifying approximations used should not cause significant errors in the computed detector responses.

3.5 Energy Deposition Spectra

While presenting the detector response in terms of PHS is useful because this is the form in which the data are obtained experimentally, it is also helpful in interpreting the response to define a variable which is more directly related to energy deposition. Therefore, we define what will be referred to as the "energy deposition spectrum" as

$$F_i \equiv \frac{n_i \, \bar{E}_i}{\delta E_i \, \Delta t \, \rho \, N_c} \quad ,$$

where

$$\bar{E}_i = (E_{i+1} + E_i)/2$$

and

$$\delta E_i = \ell og_{10} \, E_{i+1} - \ell og_{10} \, E_i \; .$$

In terms of the PHS,

$$F_i = N_i \, \bar{E}_i \, \frac{\Delta E_i}{\delta E_i} \quad ,$$

and the total energy deposition is

$$\varepsilon = \sum_i N_i \, \bar{E}_i \, \Delta E_i = \sum_i F_i \, \delta E_i \; .$$

To show the detector response over a wide range of energies, it is necessary to use a logarithmic energy scale. Therefore, F_i is defined so that when a logarithmic scale is used for energy and a linear scale for F_i, the area under the F_i curve is the total energy deposition. (For all of the results here, equal logarithmic energy intervals are used with 10 intervals per decade, so $\varepsilon = 0.1 \sum_i F_i$.)

Note that the definition of F_i above is equivalent to defining a new energy variable $E' = \ell og_{10}\ E$ and defining the energy deposition spectrum as

$$F(E')\,dE' \equiv E\,N(E)\,dE$$

or

$$F(E') = \alpha\ E^2\ N(E)\ ,$$

where

$$\alpha = \ell n\ x/\ell og_{10}\ x\ .$$

Figure 7 shows energy-deposition spectra for various detector thicknesses. The area under the spectra for individual particle types is the energy deposited by that particle type. The uncorrelated spectrum is the sum of the spectra for individual particle types. The total correlated spectrum includes energy correlations and corresponds to the spectrum that would be obtained from a measured pulse-height spectrum.

From fig. 7 observe that the relative position in energy at which protons and heavy particles contribute changes with detector thickness. For example, for $\Delta t = 50\ \mu$ the proton and heavy-particle contributions are fairly well resolved, whereas for $\Delta t = 3000\ \mu$ protons and heavy particles contribute at the same energies. The recoil contribution, which is very small for all thicknesses, occurs at about the same energies for all Δt since the recoil contribution even for the thinnest detectors is dominated by the captures within the detector. As Δt increases and a larger portion of the captures takes place within the silicon, the relative contribution of heavy particles decreases because, as mentioned previously, the alpha-particle production is much less for captures in silicon than in tissue.

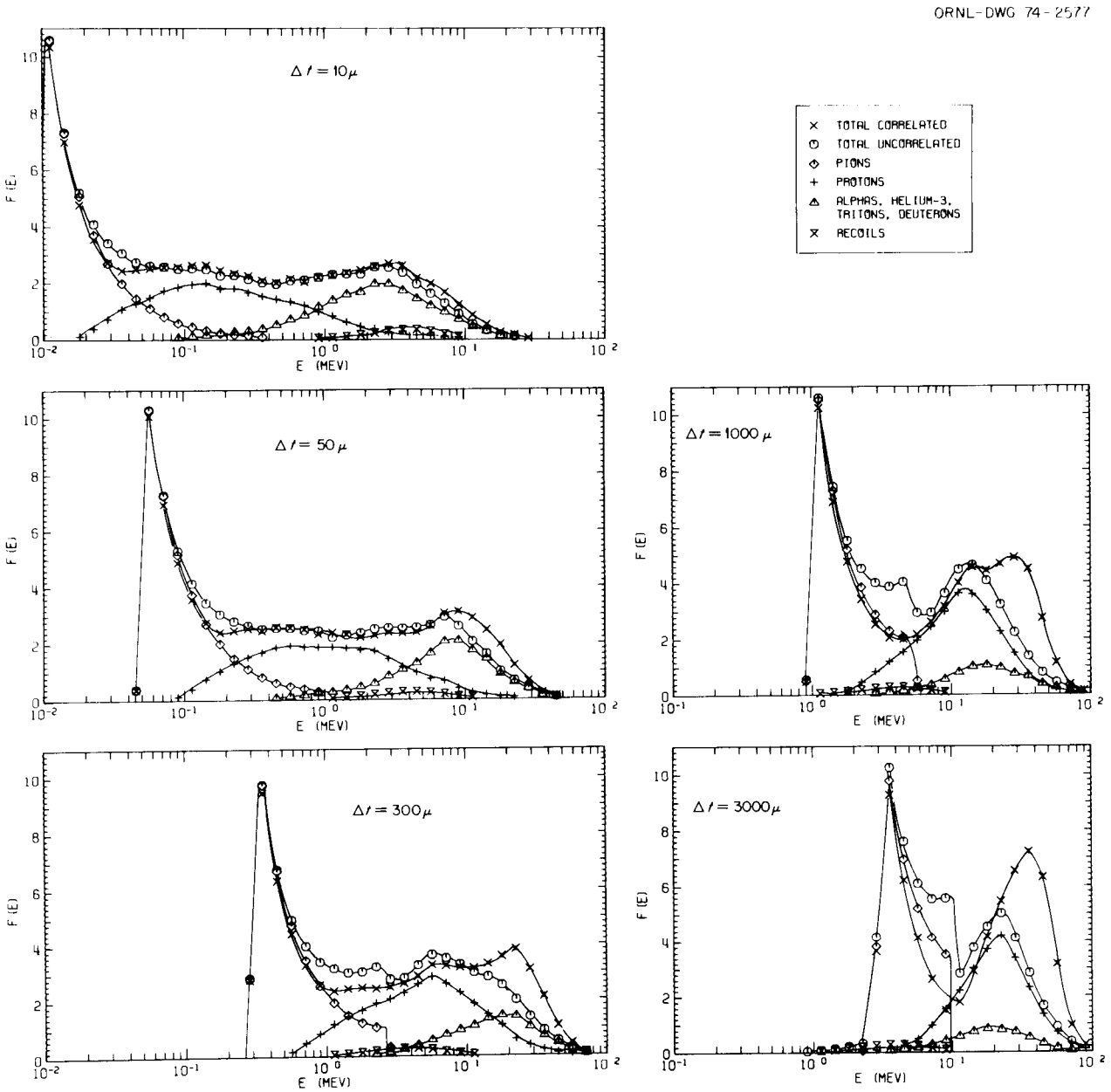

Fig. 7. Energy deposition spectra for silicon detectors of various thicknesses. F(E), defined in text, has units of $MeV \cdot g^{-1} \cdot cm^2 \cdot capture^{-1} \cdot (\log_{10}$ energy interval$)^{-1}$.

Figure 7 shows that for thin detectors the correlated and uncorrelated spectra are quite similar, but there is little resemblance between the correlated and uncorrelated spectra for thick detectors. Therefore, in determining the effect of a particular particle type on the total correlated spectrum for thick detectors, the uncorrelated spectra for individual particle types are of little use. One way of indicating the effect of individual particle types for thick detectors is to compute the spectrum that would be obtained if the particle type of interest did not contribute at all and compare this spectrum with the total spectrum. For example, to see the effect of pions, a "total minus pion" spectrum is computed in which energy correlations are taken into account but energy deposition by pions is ignored. Such spectra are shown in fig. 8 for $\Delta t = 1000\ \mu$. The difference in area under the two curves in each case corresponds to the energy deposition by that particle type. The high-energy peak is due mainly to the highly correlated contributions of protons and heavy particles. Also, fig. 8 shows that for thick detectors the pions not only produce the large peak at low energies but have an appreciable effect at all energies. Thus, while for thin detectors the energy depositions from different particle types are fairly well resolved so that certain portions of the total spectrum can be identified with certain types of particles, this is not at all the case for thick detectors.

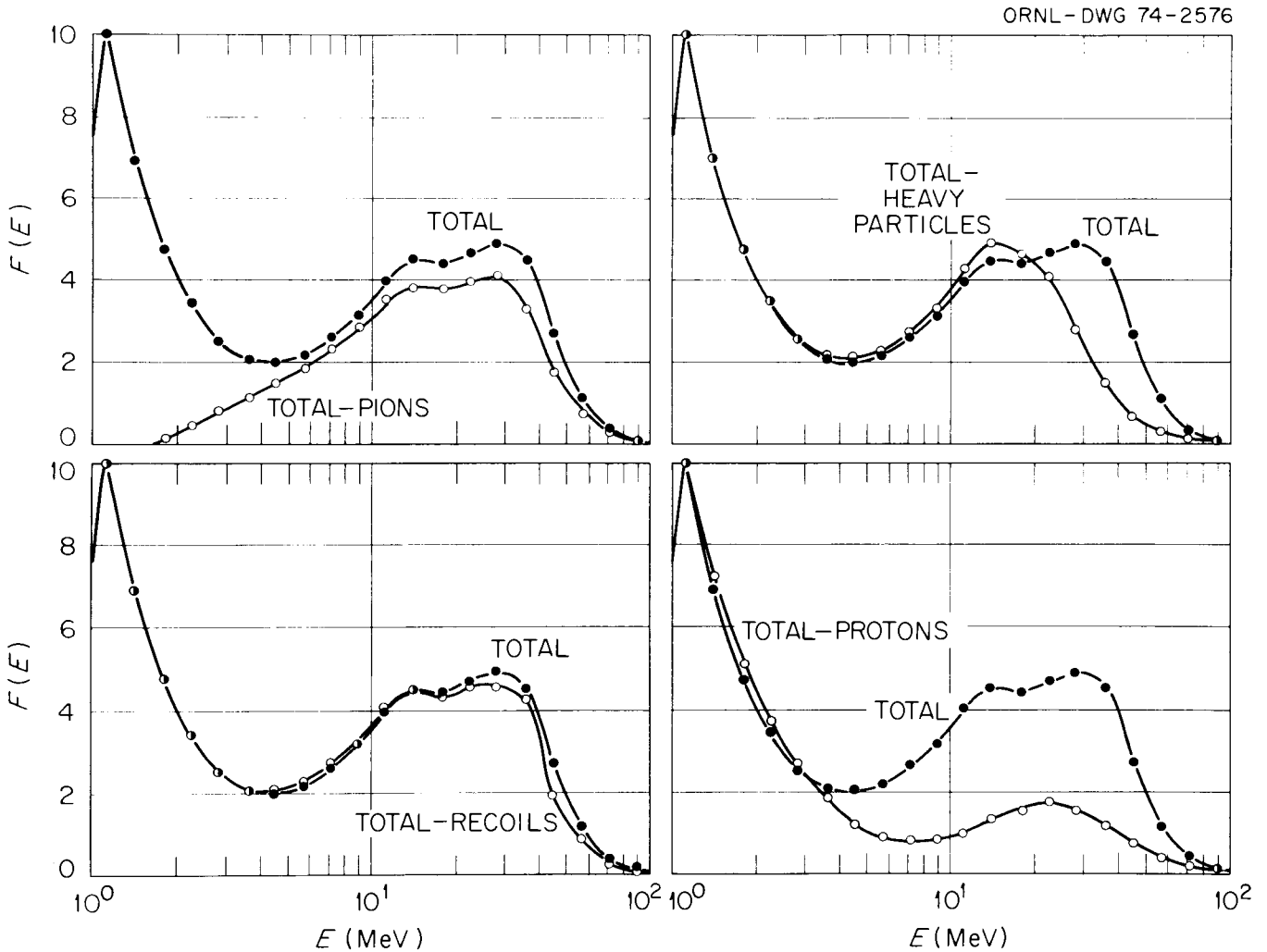

Fig. 8. Energy deposition spectra for silicon detector 1000 μ in thickness.

3.6 Inferring Tissue Energy Deposition From Detector Response

We now consider the problem of estimating the tissue energy deposition from the silicon PHS. It is assumed that only the total correlated PHS (and its associated energy deposition spectrum) is known as this corresponds to the experimental data that would be available. Other results, such as the contribution of various particle types to the silicon energy deposition and the actual tissue energy deposition computed, will not be used directly but only for guidance.

There are several approaches which might be used, and by having computed the actual tissue energy deposition, the accuracy of different procedures can be evaluated. We consider here only one method which, although approximate, is rather simple. Only the thin (Δt = 10 and 50 μ) detectors will be considered since it has been shown that the contribution of individual particle types cannot be easily identified from the total spectrum for thick detectors.

First, consider the 10-μ detector and the problem of estimating from the total spectrum the energy deposition in silicon by various particle types. Since the contribution from recoils is small and since even for thin detectors the recoil contribution cannot be identified from the total spectrum, recoils and heavy particles will be taken as one particle category. Thus, we have only three particle categories: pions, protons, and heavy particles plus recoils. We now assume that the low-energy peak in the total energy-deposition spectrum (fig. 7) is due entirely to pions, the high-energy peak is due entirely to heavy particles and recoils, and the remaining energy deposition is due to protons. The assumed pion contribution is obtained by extrapolation as shown in fig. 9. (In fig. 9 the total spectrum is the same

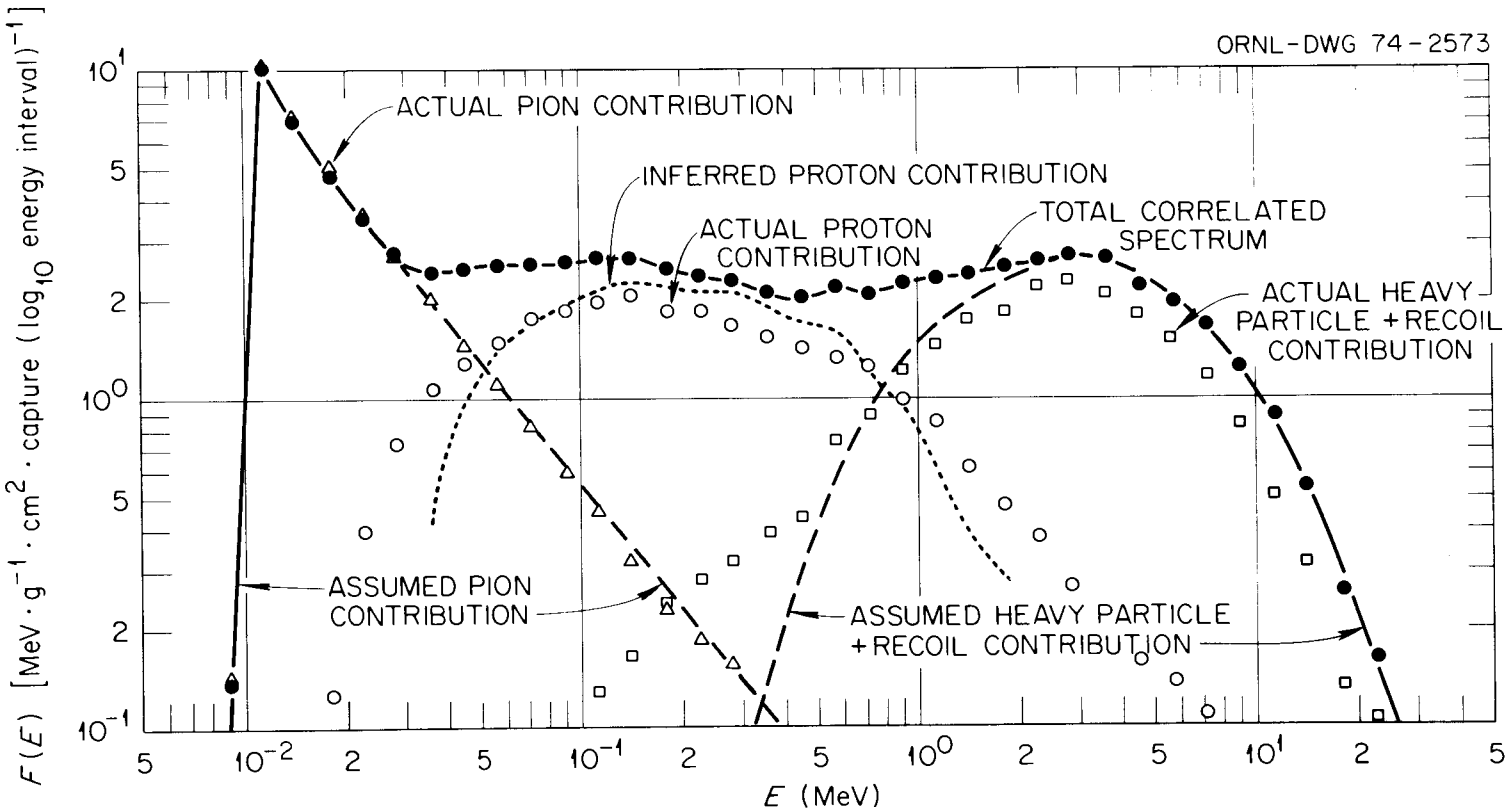

Fig. 9. Energy deposition spectra for $\Delta t = 10\ \mu$. The dashed lines are extrapolations used in estimating the pion and the heavy-particle-plus-recoil energy deposition. The dotted line is the inferred proton spectrum. The points represent actual spectra.

as that shown in fig. 7, but in fig. 9 a logarithmic ordinate scale has been used to facilitate the extrapolation.) The curve for the heavy-particle-plus-recoil contribution is obtained by considering the total spectrum at energies past the high-energy peak (at 2.8 MeV) to be entirely due to heavy particles plus recoils and that the shape of the heavy-particle-plus-recoil curve is symmetric about the high-energy peak. The pion and the heavy-particle-plus-recoil energy depositions are determined by integrating each curve, and each curve is subtracted from the integral of the total spectrum to obtain the proton energy deposition. The actual energy-deposition spectra (same as in fig. 7) are also shown in fig. 9 for comparison with the assumed distributions. The estimated energy deposition in silicon obtained by this procedure is given in Table 4 under the heading "silicon, inferred." For comparison, the actual energy deposition in silicon is also listed in Table 4. (The values given in Table 4 for the actual silicon energy deposition differ very slightly from the values given earlier for $\Delta t = 10\ \mu$ in Table 3. The values in Table 4 were obtained by numerical integration of the energy-deposition spectra in fig. 7, whereas the values in Table 3 were computed by summing the energy depositions for each particle and do not involve the use of a finite energy grid.)

We now estimate the energy deposition in tissue from the inferred energy deposition in silicon. The results of the detailed calculations, Table 3, show that, as a first approximation, for thin detectors ($\Delta t = 10\ \mu$ and $50\ \mu$) the energy deposition by each particle type (except recoils) is due to particles from captures in tissue passing through the silicon rather than from particles produced by captures within the silicon. Thus, we consider the ratio of the mass stopping power in tissue to the mass stopping power in silicon and use this ratio to convert the energy deposition from

TABLE 4

Energy Depositions[a] for 10-μ Detector

Particle Type	Silicon, Actual	Silicon, Inferred	Tissue, Inferred	Tissue, Actual
Pions	3.7	3.6	4.7	4.7
Protons	2.8	2.6	3.4	3.8
Heavy Particles and Recoils	2.3	2.6	3.6	3.7
Total	8.8	8.8	11.7	12.2

a. In units of MeV per unit detector thickness in g cm^{-2} per π^- capture.

silicon to tissue. The stopping-power ratio, computed using the SPAR code[8]) is shown in fig. 10 as a function of energy for pions, protons, and alpha particles. A proper average stopping power for each particle type could be obtained using the energy spectra of the particles hitting the detector, and these spectra are available from the calculations. However, in experiments these spectra will not usually be known. To obtain an average ratio for protons, we arbitrarily use the ratio at the average production energy. From Table 1, protons from π^- capture in tissue have an average energy of 16.3 MeV, and from fig. 10 the stopping-power ratio for protons at this energy is about 1.3. For converting the energy deposition by heavy particles and recoils, we arbitrarily use the alpha-particle stopping-power ratio evaluated at the average heavy-particle production energy, which, from Table 1, is 11.1 MeV. From fig. 10, the stopping-power ratio for alpha particles at this energy is about 1.4. To convert the energy deposition by pions, we use a stopping-power ratio of 1.25, which is the ratio at an average pion energy of 11.5 MeV. It should be noted that while the energies for evaluating the stopping powers have been arrived at in a somewhat arbitrary manner, fig. 10 shows that over a rather large energy range the stopping-power ratios are slowly varying, and therefore the ratios are not very sensitive to the energy spectrum of the particles hitting the detector. The average energy of the particles hitting the detector will be larger than the average production energy because of the preferential slowing down of low-energy particles before reaching the detector. In fact, the average proton and average heavy-particle energies at the detector surface have been computed and are 34.8 MeV and 14.9 MeV, respectively, as compared to the average production energies of 16.3 and 11.1 MeV. However, because the stopping-power ratios are slowly varying with energy, the ratios

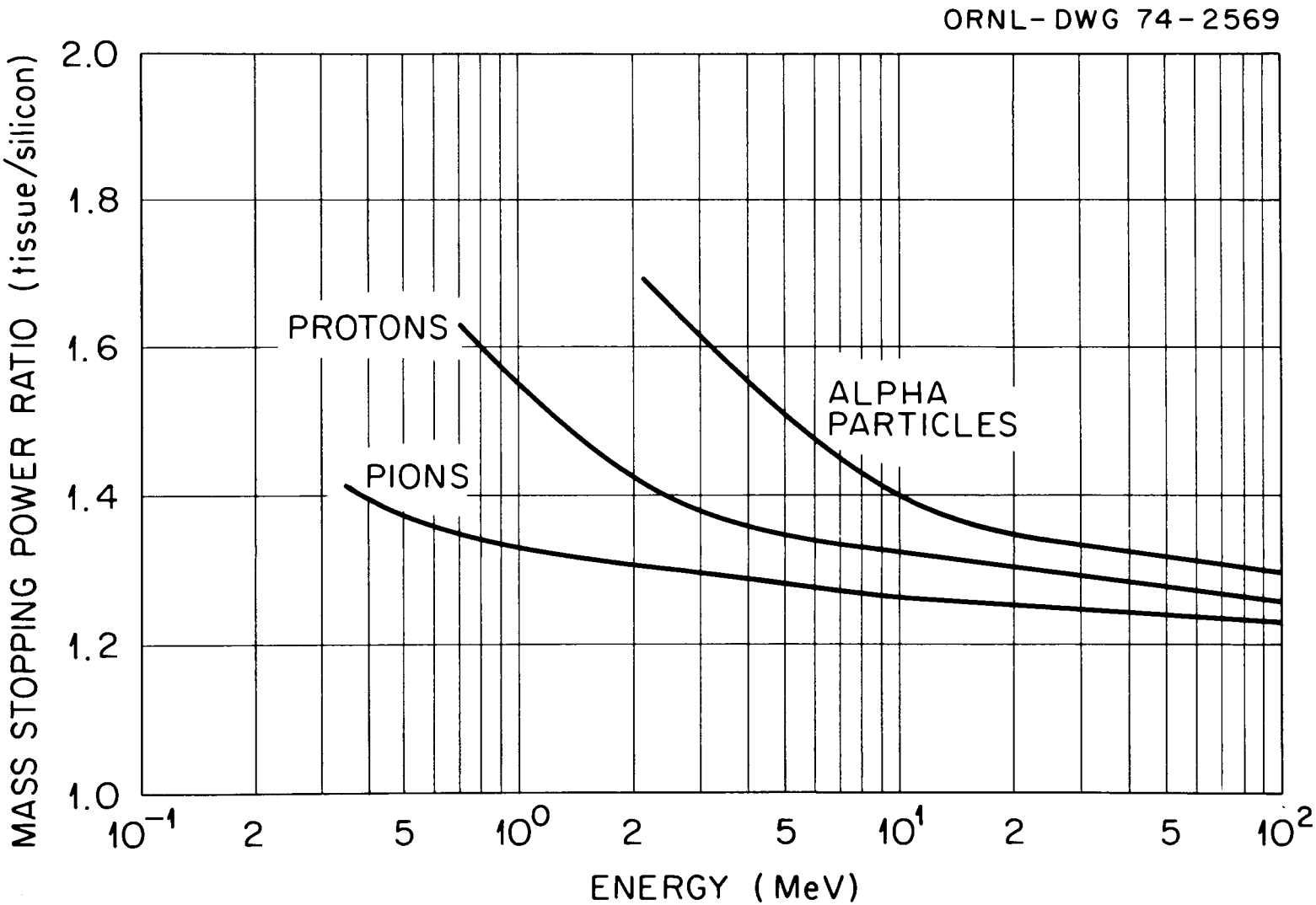

Fig. 10. Mass stopping power of tissue divided by mass stopping power of silicon. The curves are stopped at low energies at the energies corresponding to ranges in silicon of 10 μ.

evaluated at the average energies at the detector are the same (within two significant figures) as the ratios at the production energies.

The magnitude of the approximations in using the above stopping-power ratios to convert silicon energy deposition to tissue energy deposition can be checked by comparison with the energy depositions actually computed. Using the data from Table 3, Table 5 gives the actual tissue-to-silicon energy-deposition ratios for various detector thicknesses and, for comparison, the approximate stopping-power ratios discussed above. The stopping-power ratios for pions and protons are in agreement with the actual energy-deposition ratios for the thin detectors, but the use of a ratio of 1.4 for converting the heavy-particle energy deposition is an underestimate. Table 5 also shows that using the heavy-particle stopping-power ratio of 1.4 for converting the recoil-energy deposition is a good approximation, but this is fortuitous since the energy-deposition ratio for recoils is governed by the ratio of recoil energy produced in tissue vs silicon rather than by the stopping-power ratio.

The energy depositions obtained by multiplying the "silicon, inferred" values in Table 4 by the approximate stopping-power ratios of 1.25, 1.3, and 1.4 for pions, protons, and heavy particles plus recoils are given in Table 4 under "tissue, inferred." The last column in Table 4 gives the actual tissue energy deposition from Table 3. Thus, this procedure for inferring the tissue energy deposition from the silicon PHS is accurate to within about 10%. Note, however, that in the two steps of this procedure (first, estimating the energy deposition in silicon, and, second, converting the silicon energy deposition to tissue energy deposition) there are compensating errors, particularly for the energy deposition from heavy particles and recoils.

TABLE 5

Ratio of Energy Deposition Per Unit Mass in Tissue to Energy Deposition Per Unit Mass in Silicon

Particle Type	Approximate Mass Stopping-Power Ratio	$\Delta t = 10\ \mu$	$\Delta t = 50\ \mu$	$\Delta t = 300\ \mu$	$\Delta t = 1000\ \mu$	$\Delta t = 3000\ \mu$
Pions	1.25	1.3	1.3	1.3	1.3	1.4
Protons	1.3	1.3	1.3	1.3	1.4	1.5
Heavy Particles	1.4	1.6	2.0	3.1	4.6	5.8
Recoils		1.4	1.6	1.7	1.8	1.8
Total		1.4	1.5	1.6	1.7	1.8

The energy deposition in tissue using the 50-μ PHS has also been estimated (see Table 6), and the accuracy is roughly the same as that for the 10-μ detector.

TABLE 6

Energy Depositions[a] for 50-μ Detector

Particle Type	Silicon, Actual	Silicon, Inferred	Tissue, Inferred	Tissue, Actual
Pions	3.7	3.5	4.6	4.6
Protons	2.8	2.7	3.5	3.7
Heavy Particles and Recoils	1.9	2.2	3.1	3.7
Total	8.4	8.4	11.2	12.0

a. In units of MeV per unit detector thickness in g cm^{-2} per π^- capture.

APPENDIX A

STOPPING POWERS AND RANGES FOR TISSUE AND SILICON

Stopping powers and ranges as generated by the SPAR code[8]) are shown in figs. A.1 - A.4 for tissue and in figs. A.5 - A.10 for silicon. All of these results include the effect of nuclear Coulomb stopping - the energy loss by the particle in elastic Coulomb collisions with the nuclei of the stopping medium. Such collisions are nonionizing and do not contribute to the response of semiconductor detectors (e.g., ref. 12). However, as shown in fig. A.11, nuclear stopping is small compared to the total (nuclear plus electronic) stopping except at very low energies, and for the wide range of particle energies in the present problem, the effect of nuclear stopping would not be expected to be appreciable. In fact, one calculation of the pulse-height spectrum for the 50-μ detector was made with nuclear stopping omitted, and the effect was negligible.

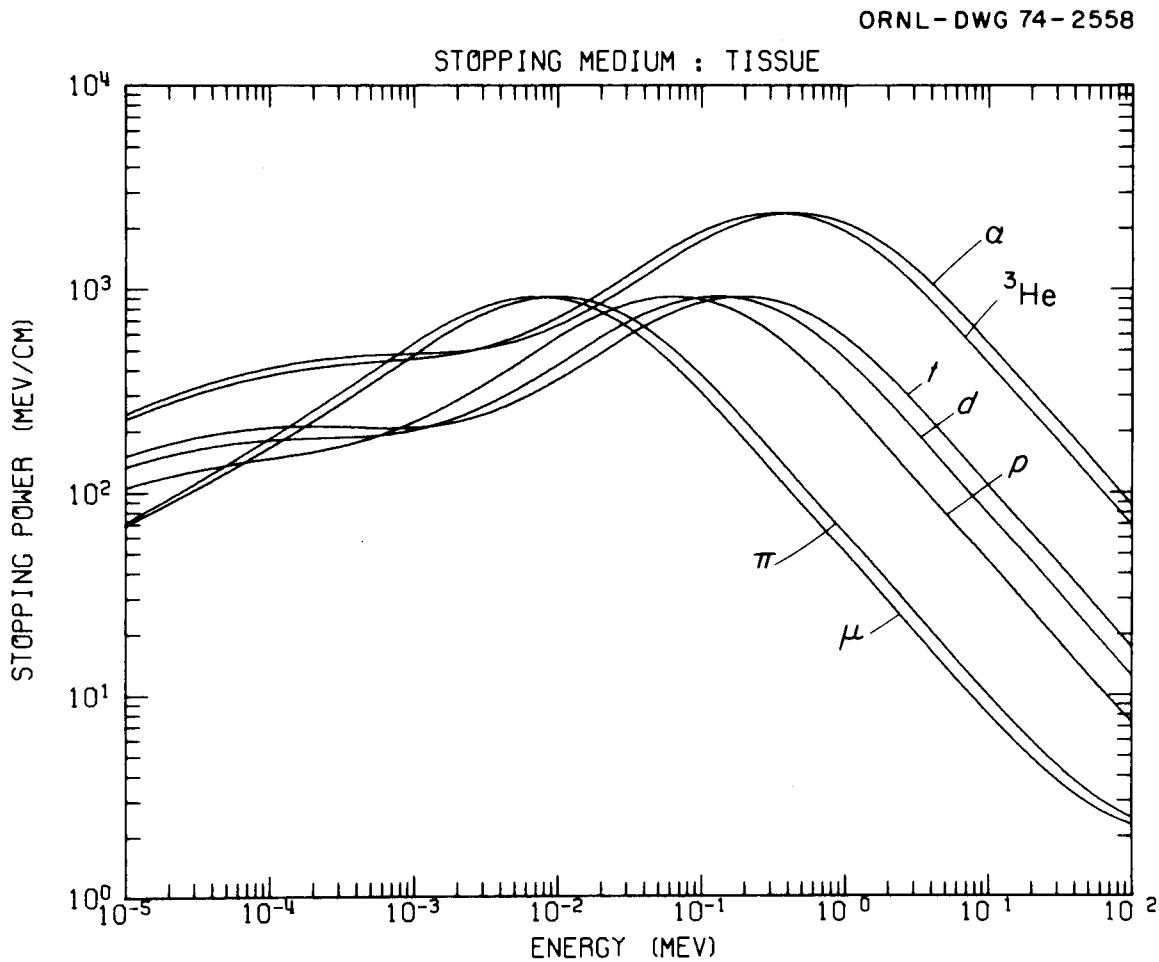

Fig. A.1. Stopping power of tissue for muons (μ), pions (π), protons (p), deuterons (d), tritons (t), helium-3 (^{3}He), and alpha particles (α).

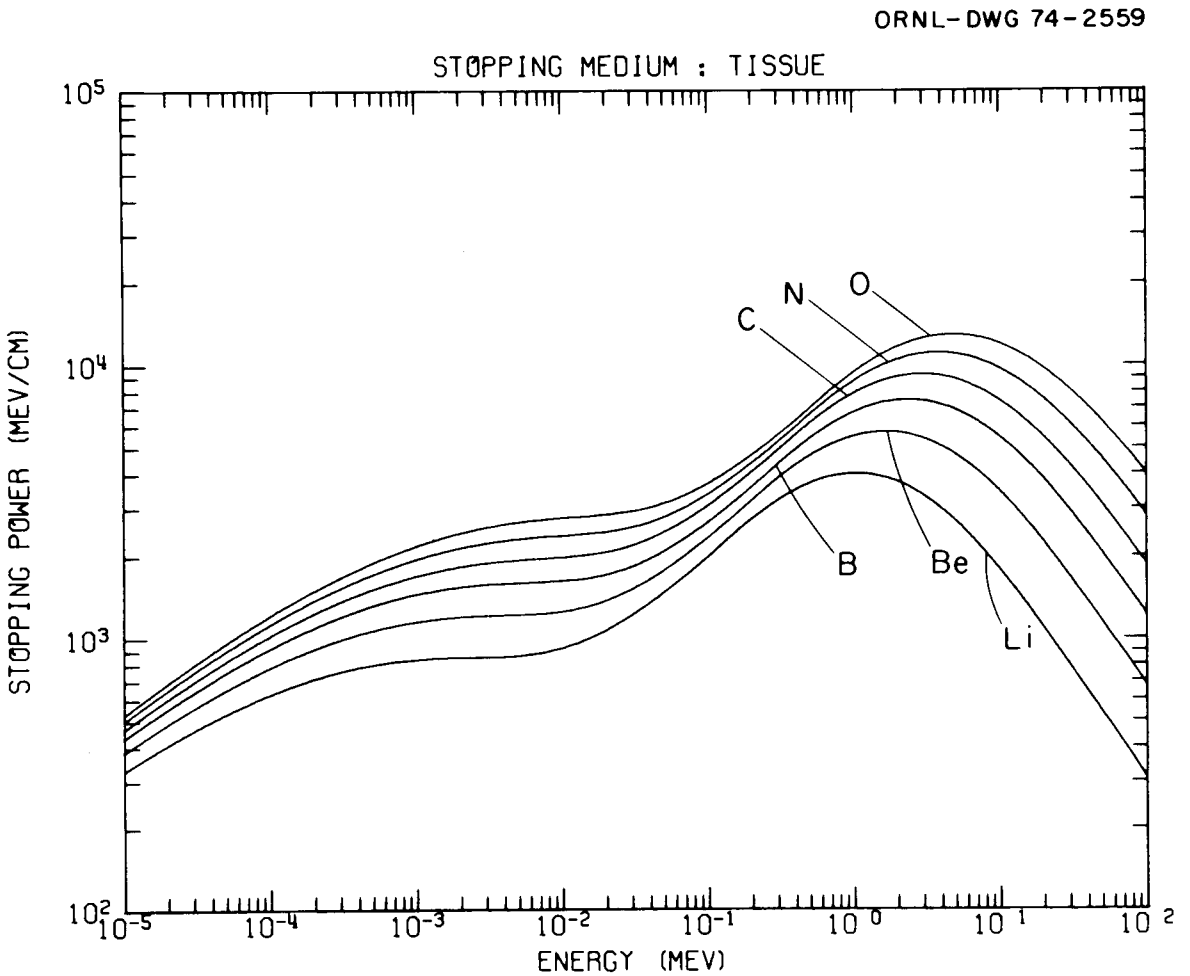

Fig. A.2. Stopping power of tissue for lithium, beryllium, boron, carbon, nitrogen, and oxygen ions.

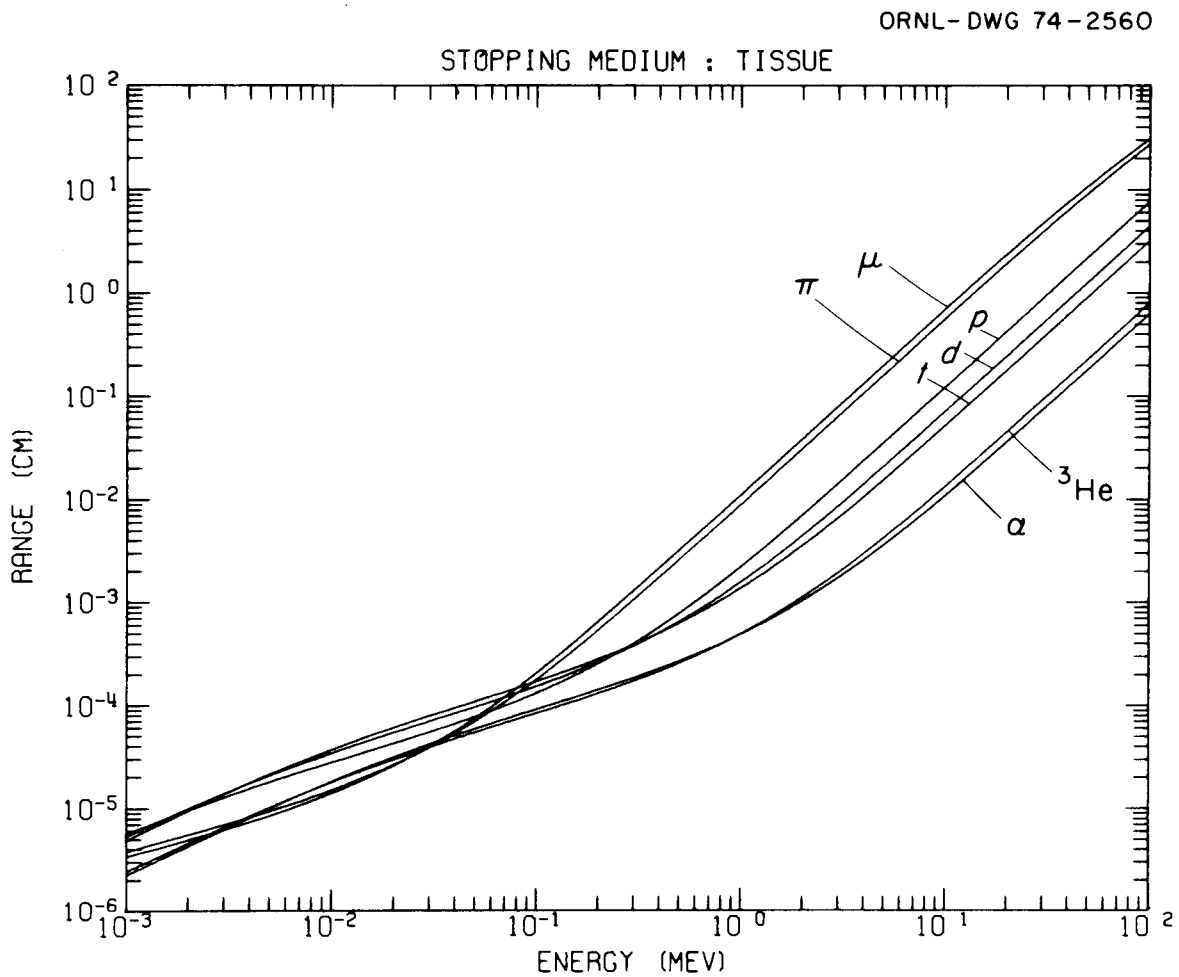

Fig. A.3. Ranges in tissue for muons (μ), pions (π), protons (p), deuterons (d), tritons (t), helium-3 (^{3}He), and alpha particles (α).

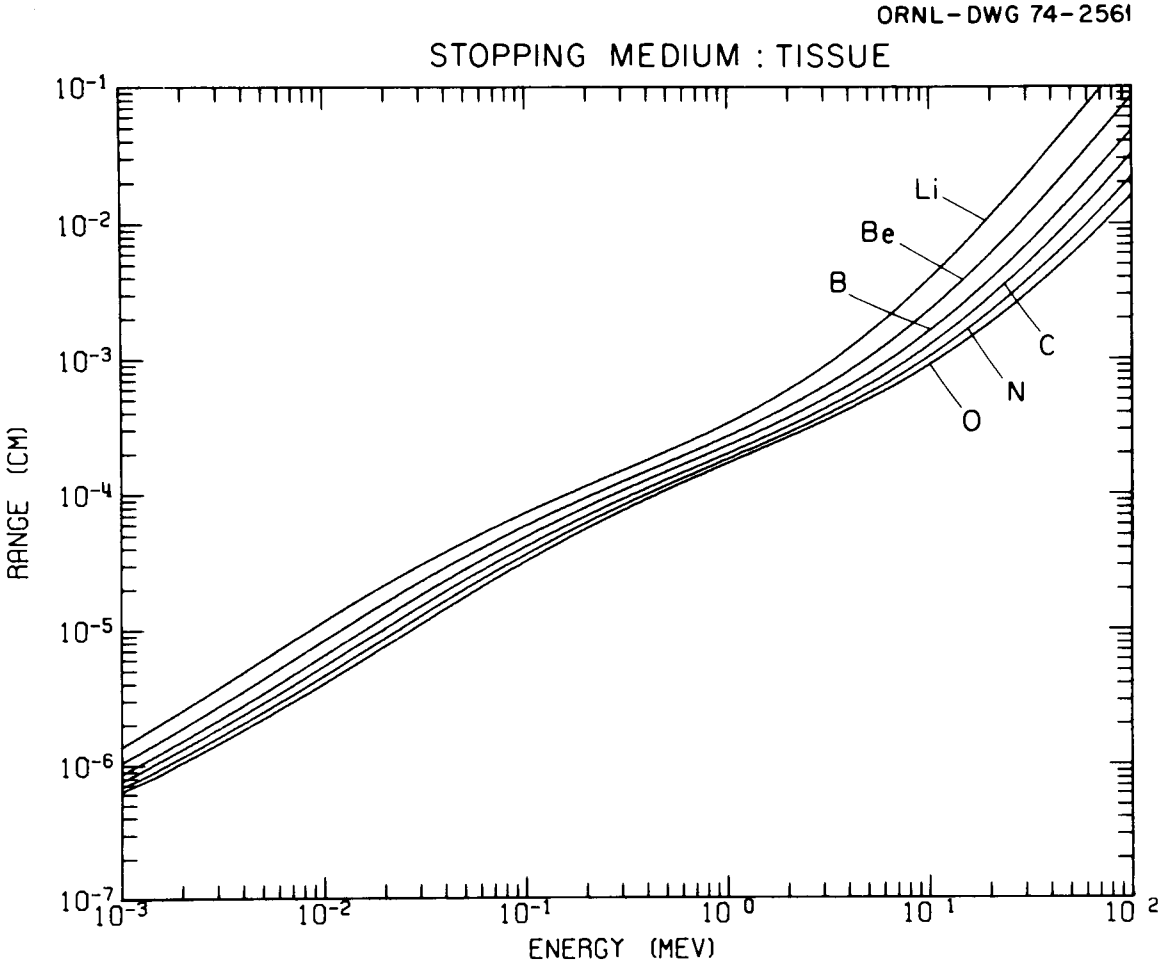

Fig. A.4. Ranges in tissue for lithium, beryllium, boron, carbon, nitrogen, and oxygen ions.

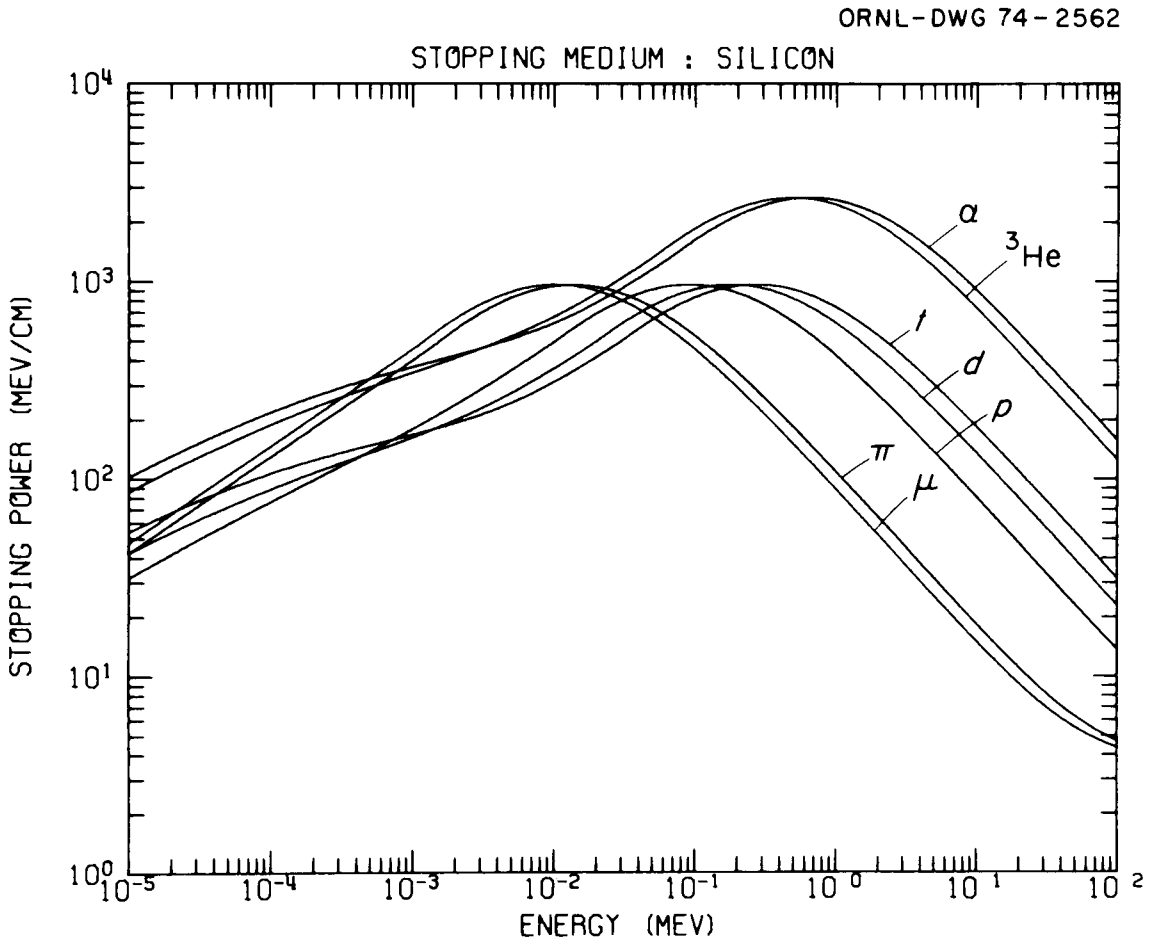

Fig. A.5. Stopping power of silicon for muons (μ), pions (π), protons (p), deuterons (d), tritons (t), helium-3 (^{3}He), and alpha particles (α).

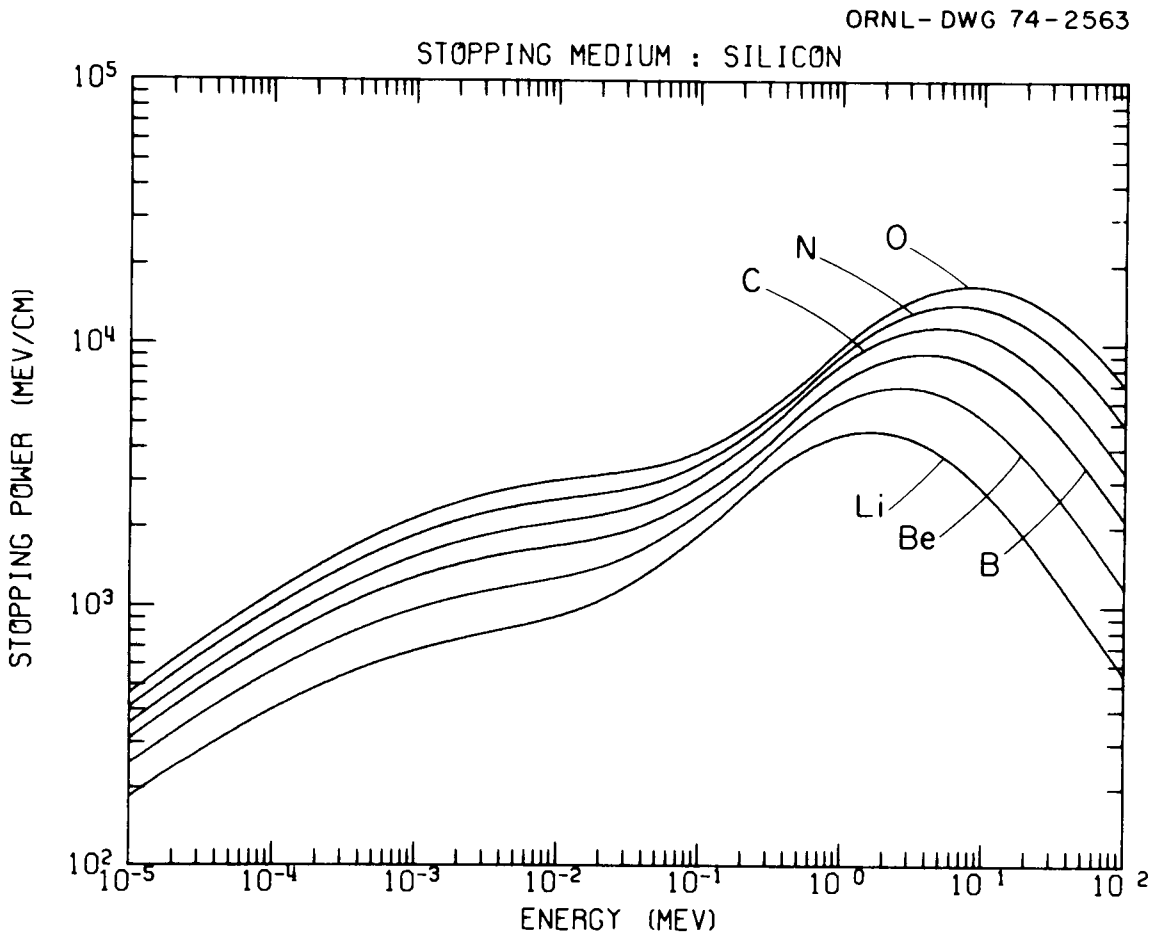

Fig. A.6. Stopping power of silicon for lithium, beryllium, boron, carbon, nitrogen, and oxygen ions.

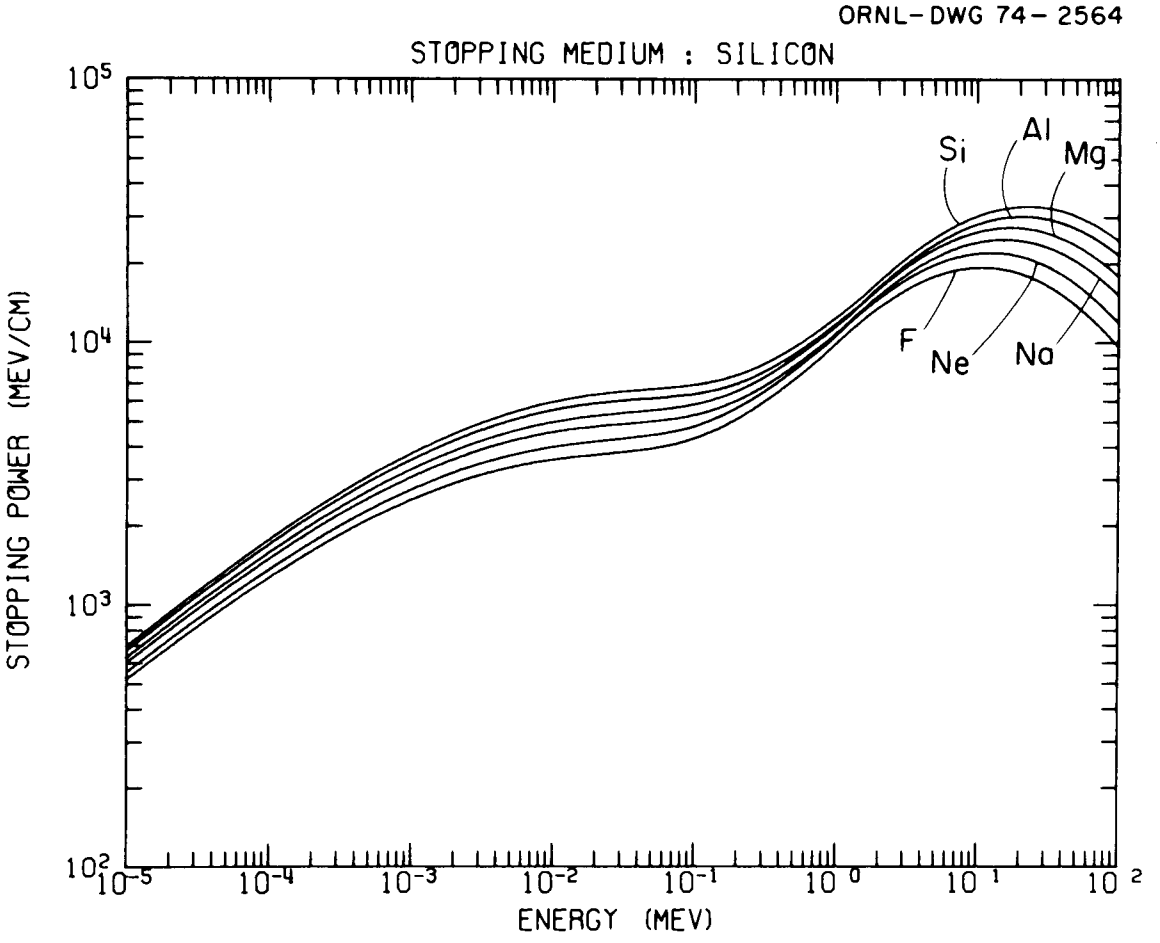

Fig. A.7. Stopping power of silicon for fluorine, neon, sodium, magnesium, aluminum, and silicon ions.

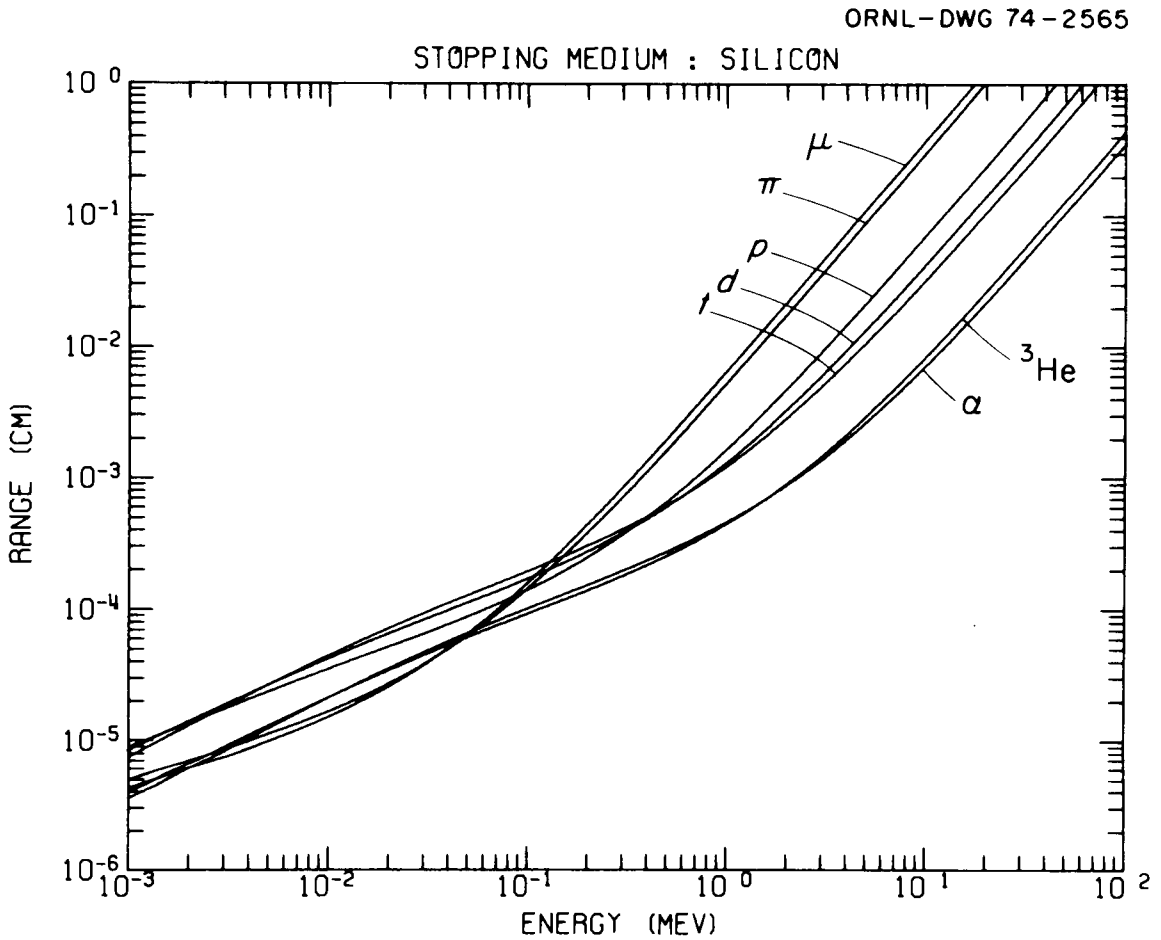

Fig. A.8. Ranges in silicon for muons (μ), pions (π), protons (p), deuterons (d), tritons (t), helium-3 (^{3}He), and alpha particles (α).

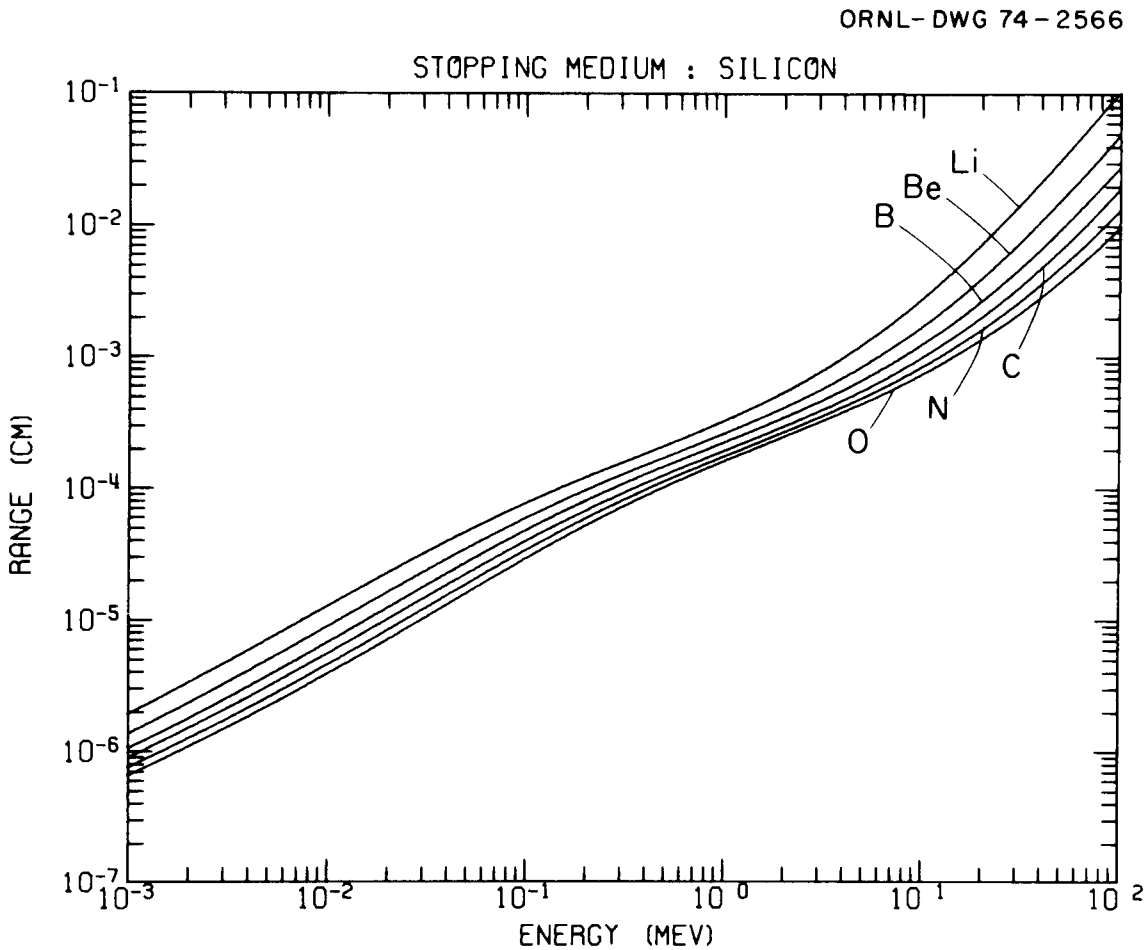

Fig. A.9. Ranges in silicon for lithium, beryllium, boron, carbon, nitrogen, and oxygen ions.

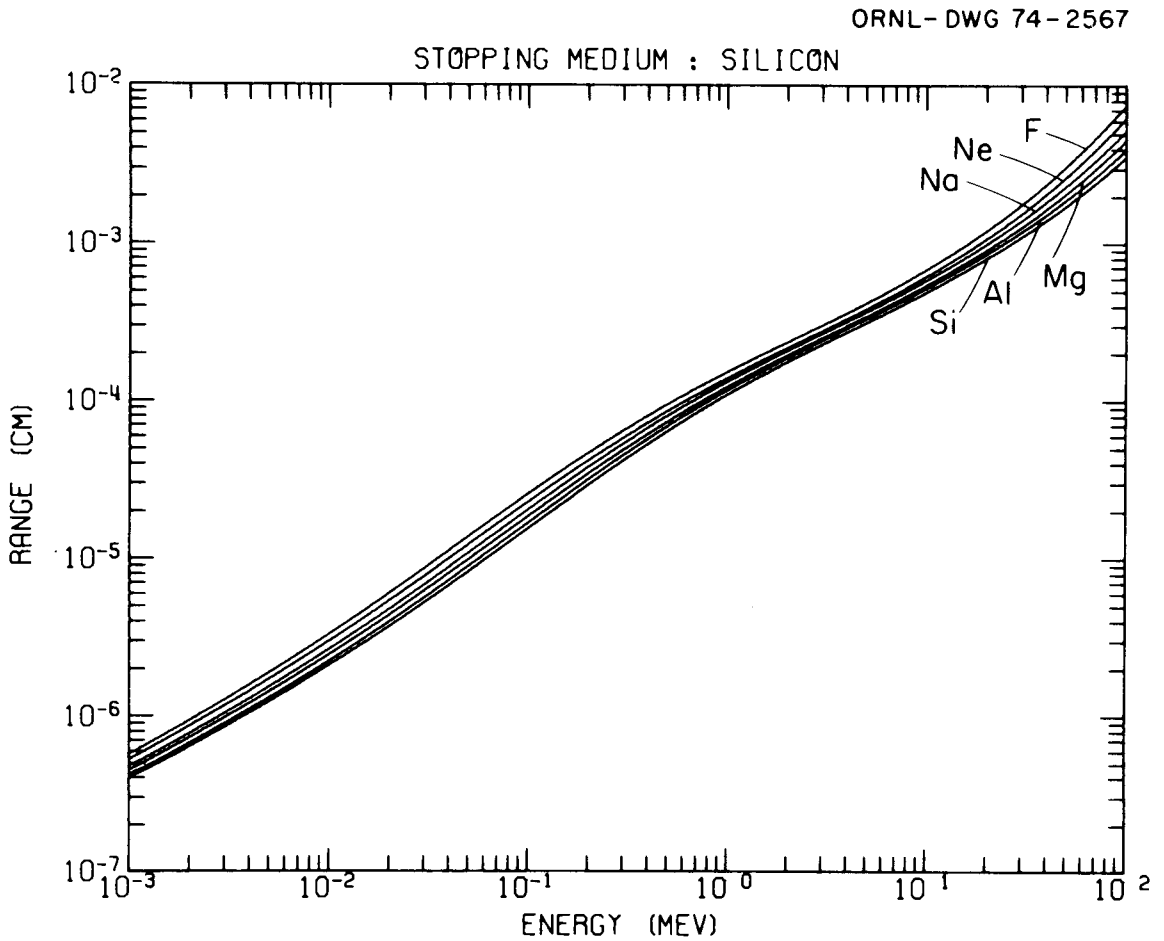

Fig. A.10. Ranges in silicon for fluorine, neon, sodium, magnesium, aluminum, and silicon ions.

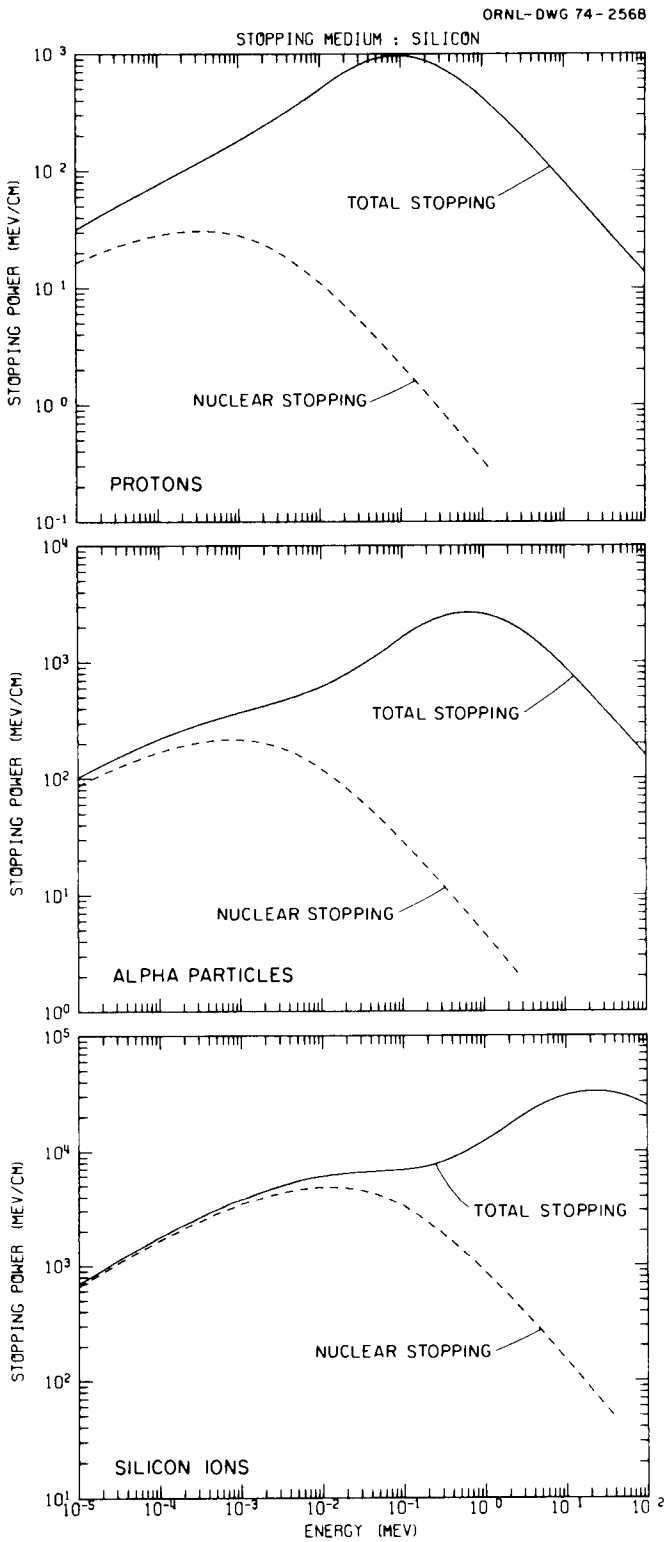

Fig. A.11. Nuclear and total (nuclear and electronic) stopping powers in silicon for protons, alpha particles, and silicon ions.

APPENDIX B

CHARGED-PARTICLE ENERGY DEPOSITION FROM π^- CAPTURES IN SILICON AND IN TISSUE

In interpreting the results given in the text, it is helpful to know the energy deposition by various capture products as a function of the distance from the π^- capture site. Figure B.1 shows the energy deposited by the slowing down of the charged particles produced from π^- captures in silicon and in tissue as a function of D, the radial distance from the capture site. These results are presented as the fraction of the energy production for each particle-type category. The energy deposition in MeV can be obtained by multiplying the fractions by the appropriate energy-production values in table 1. Although various particle types are grouped in presenting the data, production energies and ranges for each individual type of particle were used in computing the energy deposition. The curves labeled "total" correspond to all charged particles and do not include the contribution from neutrons emitted by the capture, which becomes appreciable at distances $\gtrsim 10^4$ microns.

Dutrannois *et al.*[13]) have calculated the total (sum for all particle types) energy deposition in water due to the products from π^- captures in oxygen [using intranuclear-cascade-model results[5])], and their results are in very good agreement with the total energy deposition for tissue given in fig. B.1.

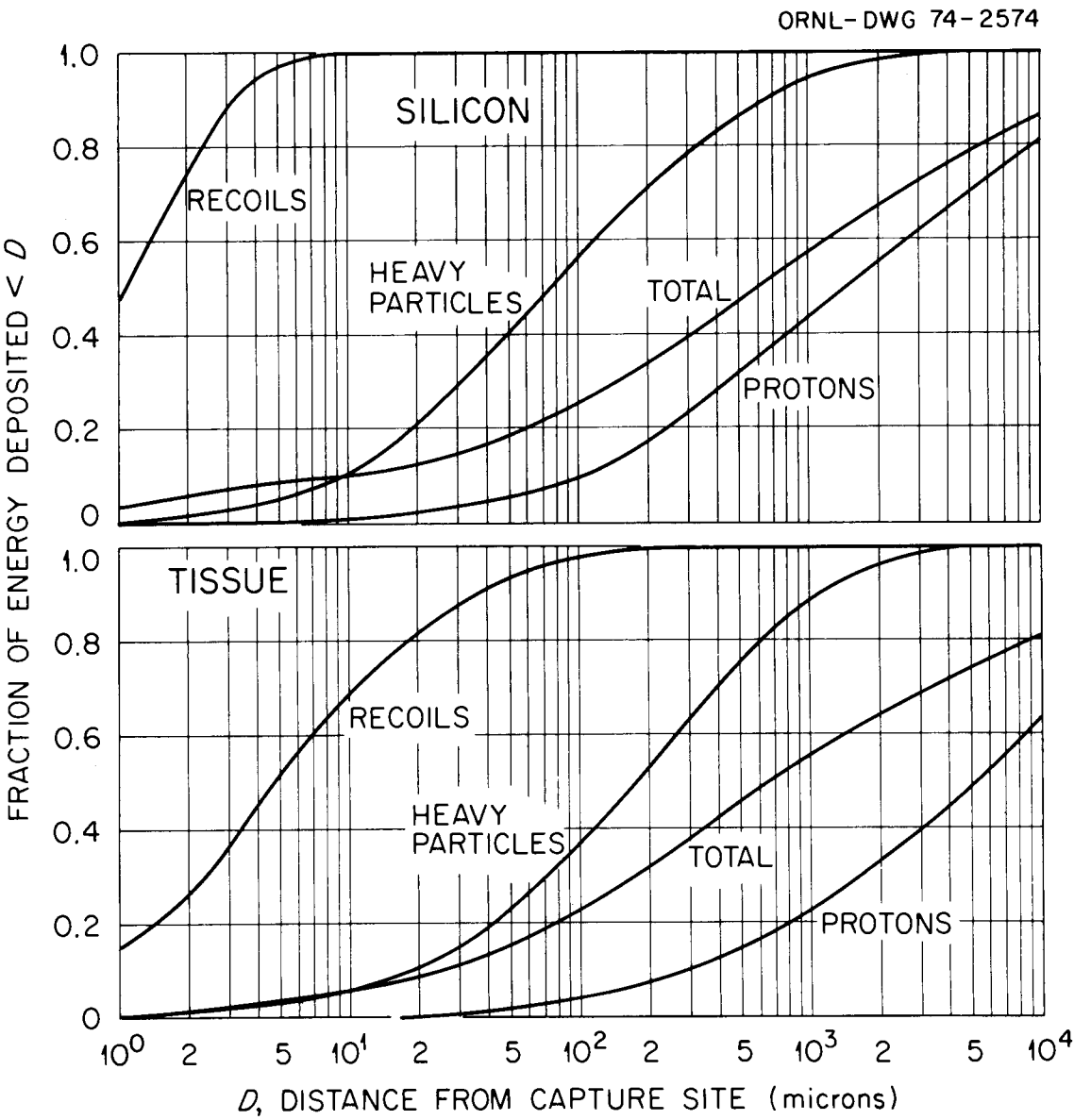

Fig. B.1. Energy deposition as a function of the distance from the π^- capture site for charged particles produced and slowing down in silicon and in tissue.

APPENDIX C

PULSE-HEIGHT SPECTRA

Pulse-height spectra like those shown in the text for $\Delta t = 50\ \mu$ and $1000\ \mu$ are shown in figs. C.1 - C.3 for $\Delta t = 10$, 300, and $3000\ \mu$.

Figures C.4 - C.6 show for $\Delta t = 10$, 50, and $1000\ \mu$ the effect of captures inside the detector on the pulse-height spectra and the difference between pulse-height spectra in silicon and in tissue. In each figure, the spectrum labeled "silicon detector, all captures" is the total correlated spectrum with captures inside and outside the detector included, and the spectrum labeled "silicon detector, captures outside" was computed with the contribution from captures inside the detector omitted. The spectrum for tissue was computed from energy depositions in tissue having the same thickness and at the same location as the silicon.

ORNL-DWG 74-3553

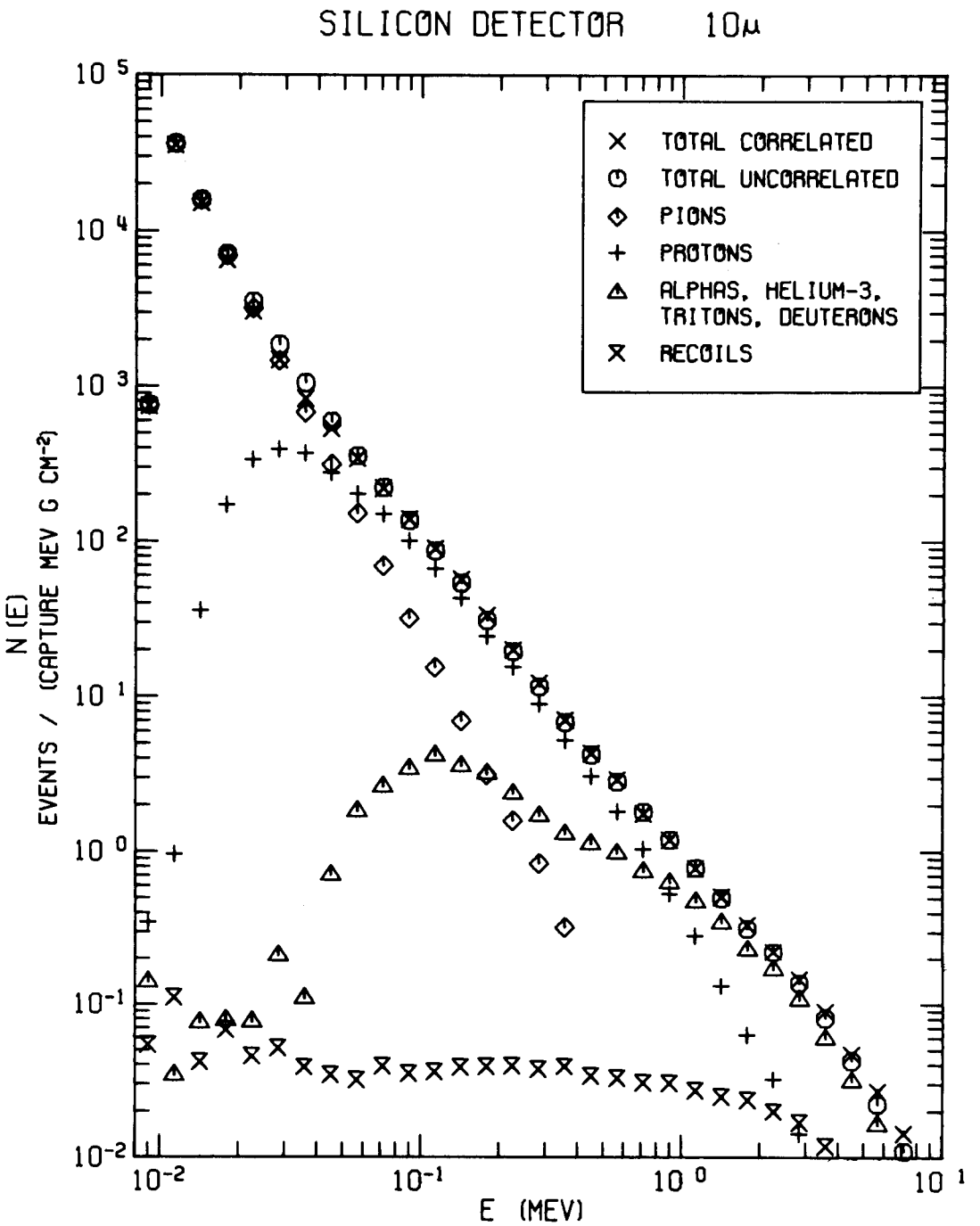

Fig. C.1. Pulse-height spectra for 10 μ silicon detector.

ORNL-DWG 74-3554

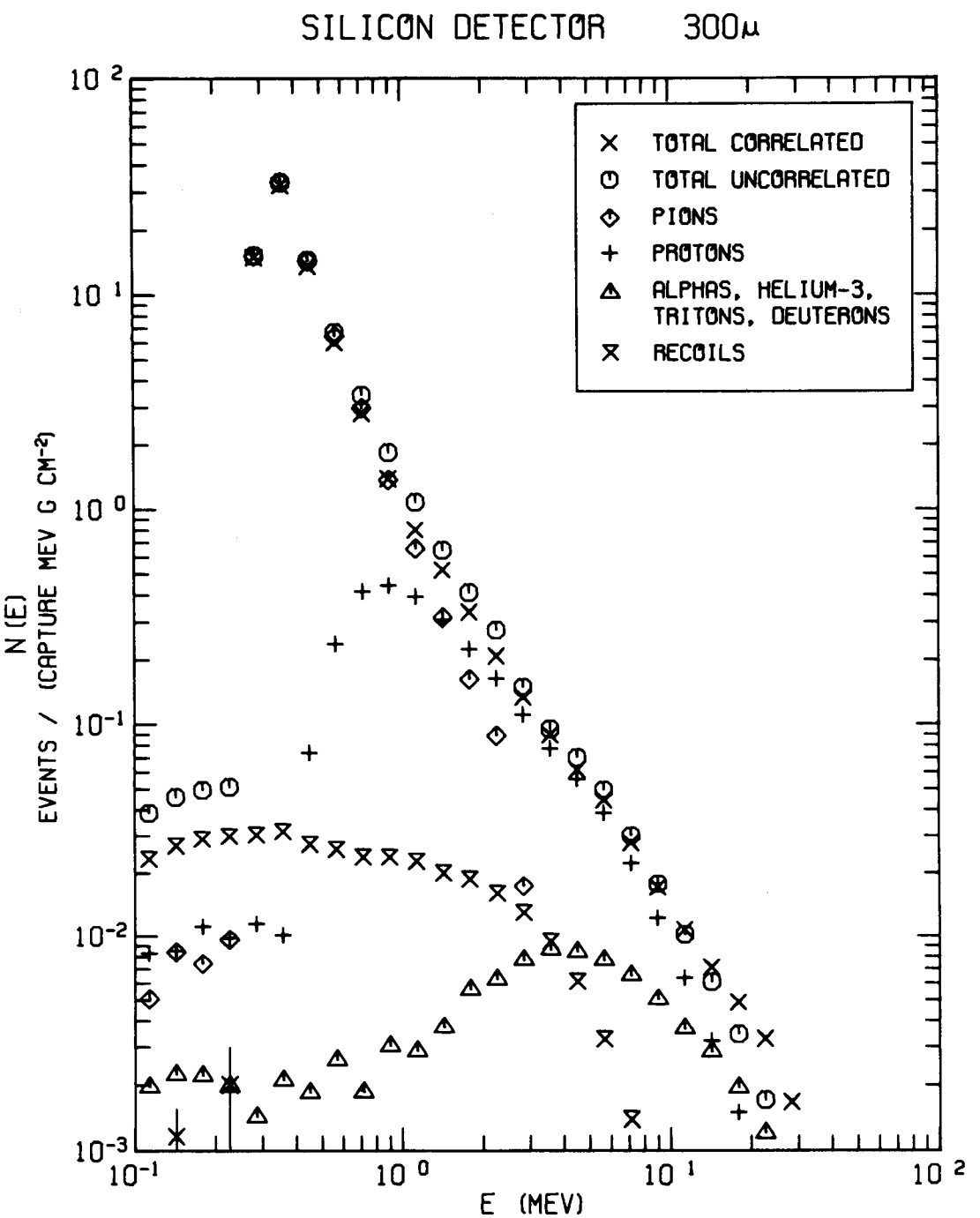

Fig. C.2. Pulse-height spectra for 300 μ silicon detector.

ORNL-DWG 74-3555

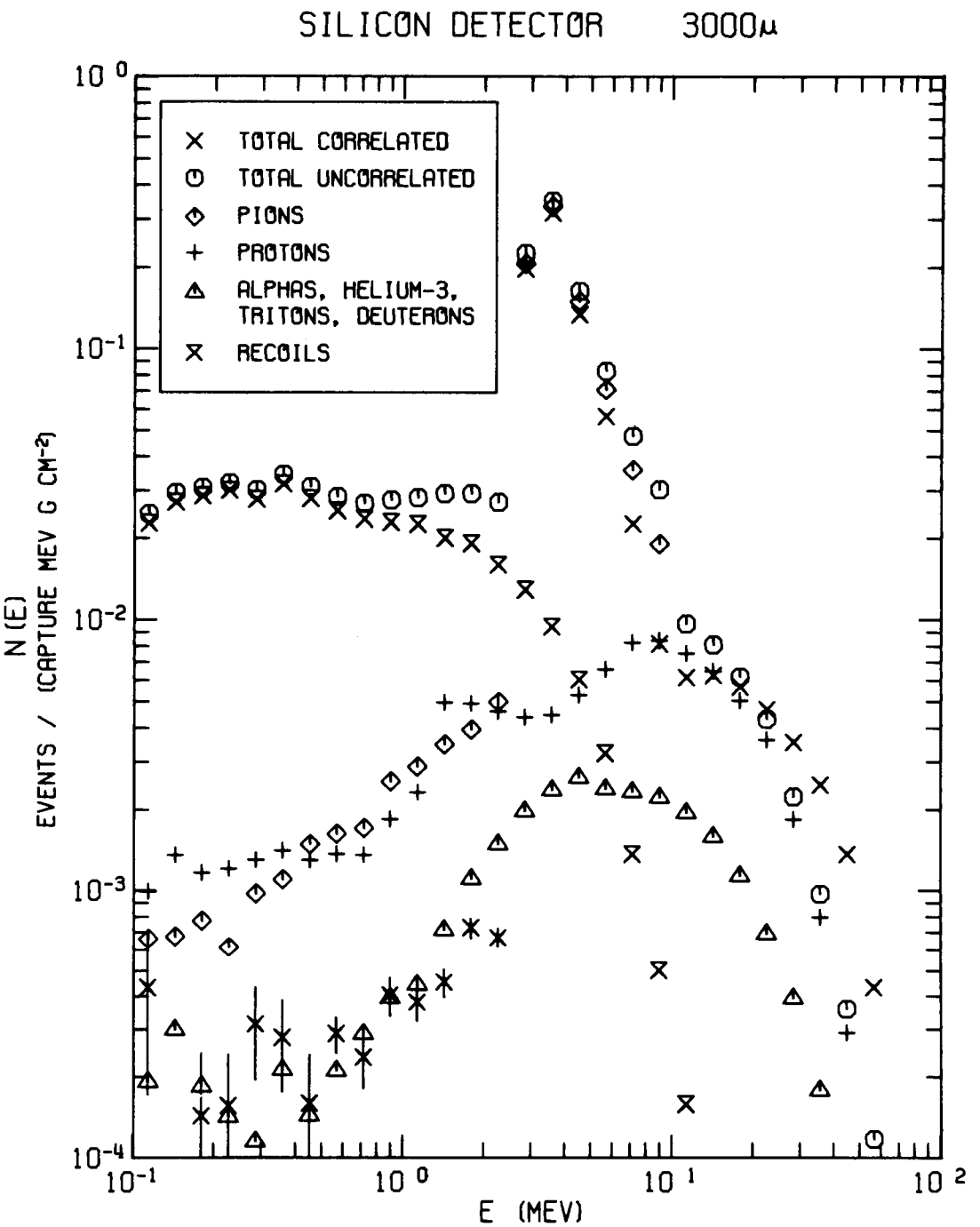

Fig. C.3. Pulse-height spectra for 3000 μ silicon detector.

ORNL-DWG 74-3556

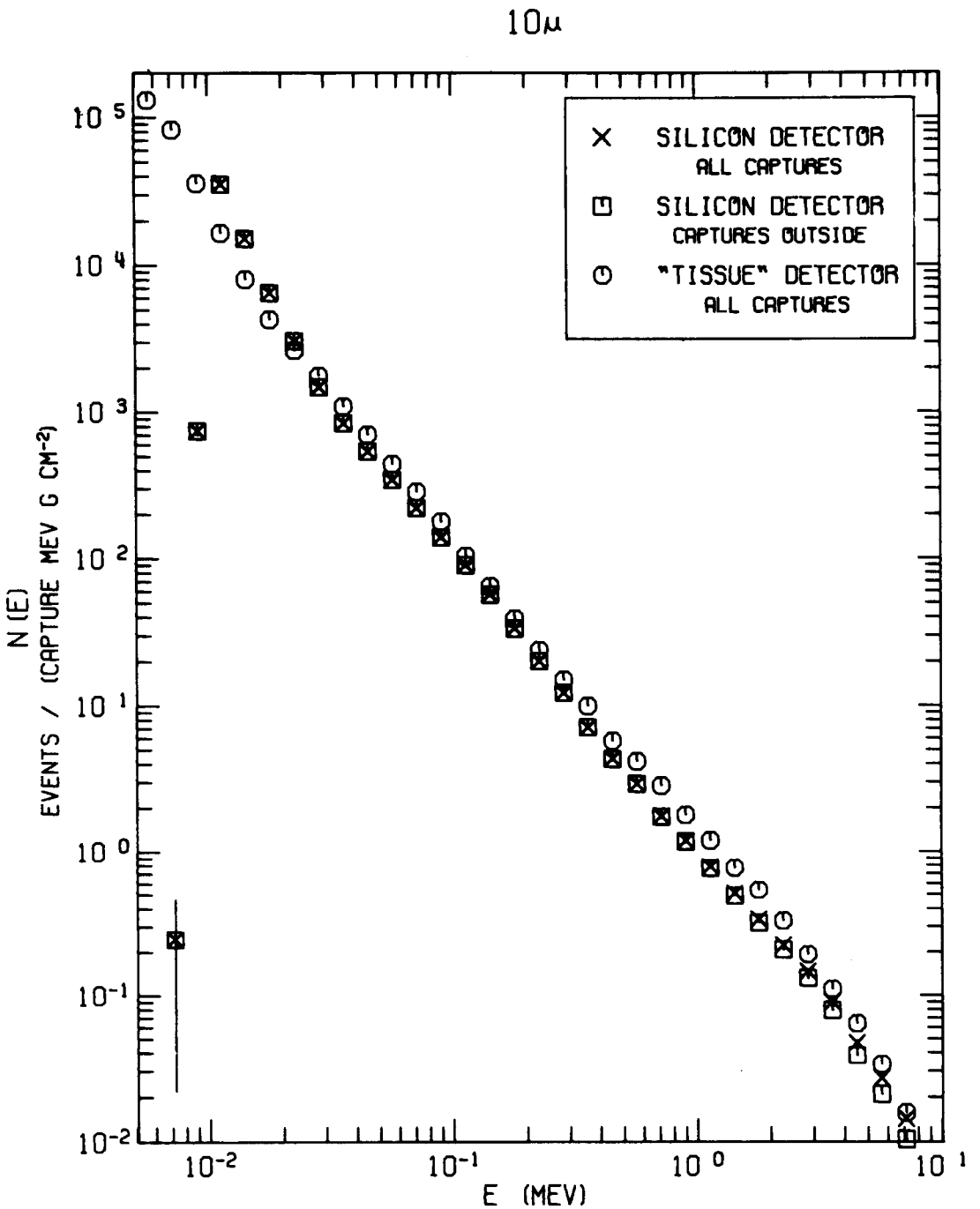

Fig. C.4. Pulse-height spectra for silicon and for tissue thicknesses of 10 μ.

ORNL-DWG 74-3557

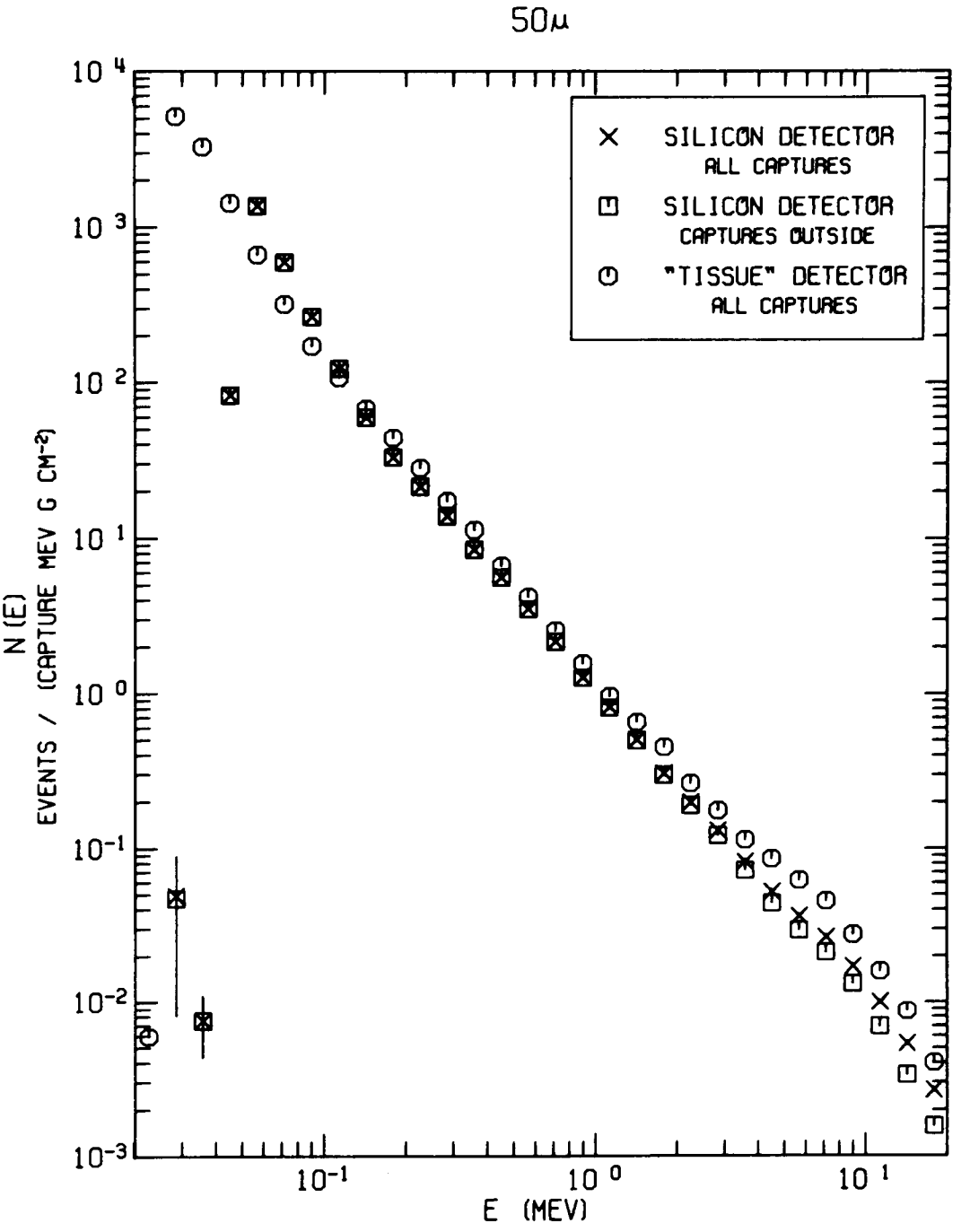

Fig. C.5. Pulse-height spectra for silicon and for tissue thicknesses of 50 μ.

ORNL-DWG 74-3558

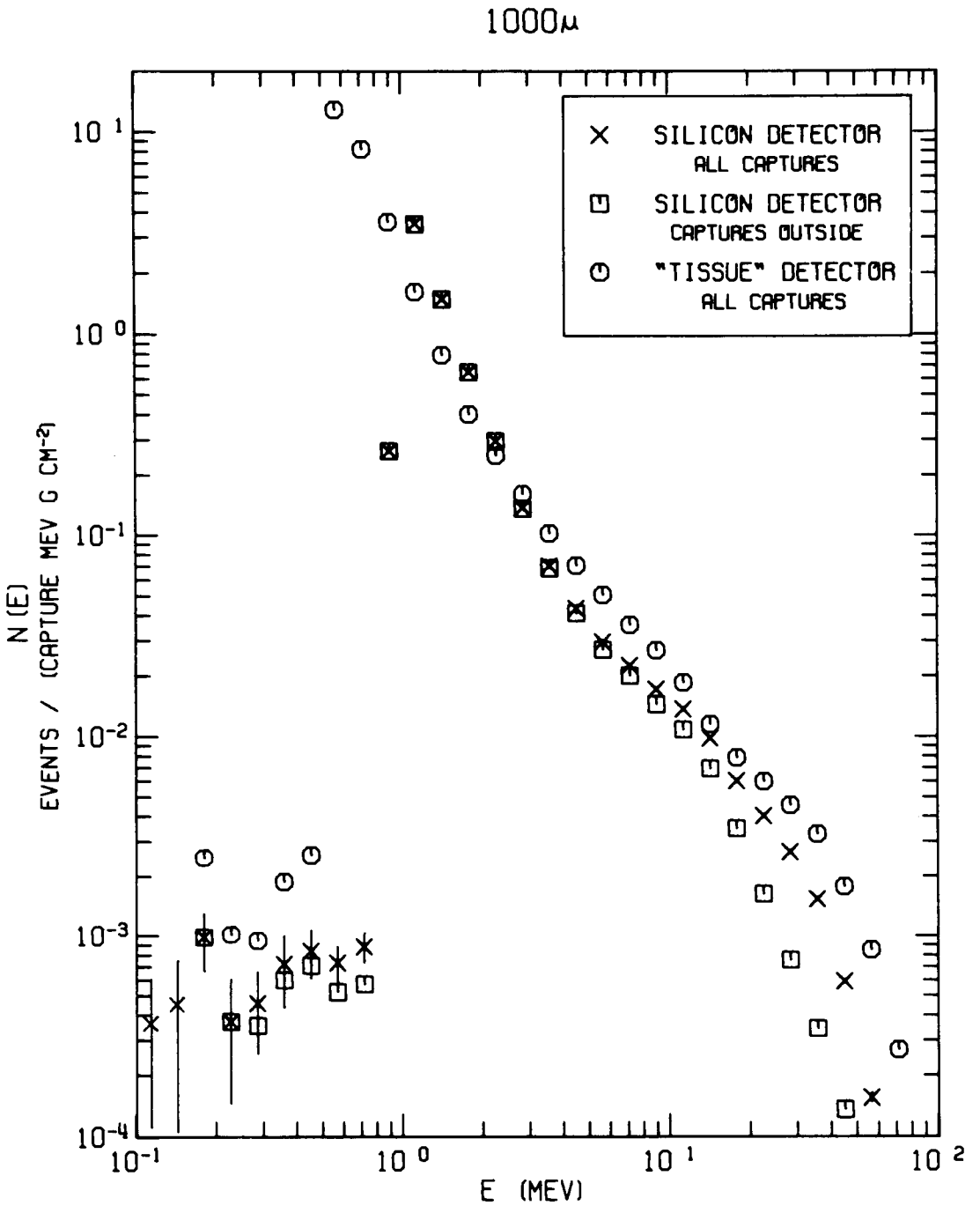

Fig. C.6. Pulse-height spectra for silicon and for tissue thicknesses of 1000 μ.

APPENDIX D

INFLUENCE OF DIFFERENCE IN CAPTURE PRODUCTS ON SILICON AND TISSUE ENERGY DEPOSITIONS

Part of the difference in the energy deposition in silicon and in tissue shown in Table 3 of the text is due to differences in stopping powers and ranges and part is due to the difference in π^- capture products from silicon and tissue. To isolate the influence of the difference in capture products, calculations were made in which, for captures taking place within the silicon, the products from π^- captures in silicon were used, but the energy deposition was computed using stopping powers and ranges for tissue. Thus, the difference between these results and those for tissue is due only to the difference in capture products.

In Table D.1 the energy depositions under the heading "tissue captures" are the same as the tissue results given in Table 3 for $\Delta t = 10\ \mu$, and the energy depositions under "silicon captures" were obtained using silicon capture products and tissue stopping powers and ranges. For the thin detectors ($\Delta t = 10$ and $50\ \mu$), the difference in capture products does not have, except for recoils, an appreciable effect on the energy deposition, but for $\Delta t \gtrsim 50\ \mu$ the difference in capture products becomes significant.

TABLE D.1

Comparison of Energy Depositions[a] for Captures in Tissue with Tissue Stopping vs Captures in Silicon with Tissue Stopping

Particle Type	Tissue Captures, Tissue Stopping	Silicon Captures, Tissue Stopping				
		10 μ	50 μ	300 μ	1000 μ	3000 μ
Pions	4.63	4.63	4.64	4.63	4.63	4.64
Protons	3.74	3.77	3.81	4.08	4.30	4.36
Heavy Particles	3.37	3.16	2.76	2.08	1.59	1.31
Recoils	0.34	0.53	0.49	0.46	0.46	0.45
Total	12.1	12.1	11.7	11.2	11.2	10.8

a. In units of MeV per unit detector thickness (in g cm^{-2}) per π^- capture.

REFERENCES

1) M. R. Raju, H. Aceto, and C. Richman, Nucl. Instr. Meth. 37 (1965) 152.

2) M. R. Raju, E. Lampo, S. B. Curtis, and C. Richman, Phys. Med. Biol. 16 (1971) 599.

3) T. W. Armstrong and K. C. Chandler, Calculated particle-production spectra from π^- captures in tissue, tissue-equivalent plastic, silicon, and germanium, Oak Ridge National Laboratory Report ORNL-TM-4462 (1974).

4) Hugo W. Bertini and Miriam P. Guthrie, Nucl. Phys. A169 (1971) 670.

5) M. P. Guthrie, R. G. Alsmiller, Jr., and H. W. Bertini, Nucl. Instr. Meth. 66 (1968) 29, with erratum Nucl. Instr. Meth. 91 (1971) 669.

6) E. Fermi and E. Teller, Phys. Rev. 72 (1947) 399.

7) Miriam P. Guthrie, EVAP-4: Another modification of a code to calculate particle evaporation from excited compound nuclei, Oak Ridge National Laboratory Report ORNL-TM-3119 (1970).

8) T. W. Armstrong and K. C. Chandler, Nucl. Instr. Meth. 113 (1973) 313.

9) Tony W. Armstrong and Kay C. Chandler, Calculations related to the application of silicon detectors in pion radiobiology, Oak Ridge National Laboratory Report ORNL-TM-4530 (1974).

10) T. W. Armstrong and K. C. Chandler, Calculations related to the application of negatively charged pions in radiotherapy: absorbed dose, LET spectra, and cell survival, Oak Ridge National Laboratory Report ORNL-TM-4294 (1973).

11) T. W. Armstrong and K. C. Chandler, Nucl. Sci. Eng. 49 (1972) 110.

[12]) E. P. Steinberg, S. B. Kaufman, B. D. Wilkins, and C. E. Gross, Nucl. Instr. Meth. 99 (1972) 309.

[13]) J. R. Dutrannois, R. N. Hamm, J. E. Turner, and H. A. Wright, Phys. Med. Biol. 17 (1972) 765.

Internal Distribution

1-3. L. S. Abbott
4. F. S. Alsmiller
5. R. G. Alsmiller, Jr.
6-40. T. W. Armstrong
41. J. A. Auxier
42. J. Barish
43. H. W. Bertini
44. A. A. Brooks
45. H. P. Carter
46-50. K. C. Chandler
51. C. E. Clifford
52. T. A. Gabriel
53. R. N. Hamm
54. T. D. Jones
55. J. L. Lucius
56. F. C. Maienschein
57. R. W. Peelle
58. R. W. Roussin
59. RSIC
60. R. T. Santoro
61. S. Siegel
62. J. B. Storer
63. D. Sundberg
64. J. R. Totter
65. J. E. Turner
66. G. E. Whitesides
67. H. A. Wright
68. A. Zucker
69. H. Feshbach (consultant)
70. P. F. Fox (consultant)
71. A. F. Henry (consultant)
72. W. W. Havens, Jr. (consultant)
73-74. Central Research Library
75. ORNL Y-12 Technical Library, Document Reference Section
76-77. Laboratory Records Department
78. Laboratory Records ORNL RC
79. ORNL Patent Office

External Distribution

80. H. Goldstein, Columbia University, New York, New York, 10027.
81. W. W. Hannum, Division of Reactor Research and Development, U. S. Atomic Energy Commission, Washington, D. C., 20545.
82. P. B. Hemmig, Division of Reactor Research and Development, U. S. Atomic Energy Commission, Washington, D. C., 20545.
83. J. L. Liverman, Division of Biomedical and Environmental Research, U. S. Atomic Energy Commission, Washington, D. C., 20545.
84. D. F. Cope, AEC Site Representative.
85. Dr. R. Vasudevan, Institute of Mathematical Sciences, Adyar, Madras, India.
86-179. Given National Science Foundation Distribution (see pp. 68-71)
180-181. Technical Information Center (TIC).
182. Research and Technical Support Division (ORO).

NATIONAL SCIENCE FOUNDATION DISTRIBUTION

1. Dr. Peter R. Almond, MD Anderson Hospital and Tumor Institute, The University of Texas, 6723 Bertner Boulevard, Houston, Texas 77025
2. Dr. Frank H. Attix, U. S. Naval Research Laboratory, Washington, D. C. 20390
3. Dr. Miguel Awschalom, Head, Research Services Section, National Accelerator Laboratory, P. O. Box 500, Batavia, Illinois 50410
4. Dr. Johan Baarli, Head, Health Physics Division, CERN, Geneva 23, SWITZERLAND
5. Dr. M. A. Bagshaw, Department of Radiology, Stanford School of Medicine, Stanford, California 94305
6. Dr. G. W. Barendsen, Radiobiological Institute of the Organization for Health Research TNO, 151 Lange Kleiweg, Rijswijk (Z-H), THE NETHERLANDS
7. Dr. Nathaniel F. Barr, Assistant Director for Measurement and Evaluation, Division of Biomedical and Environmental Research, U. S. Atomic Energy Commission, Washington, D. C. 20545
8. Dr. H. F. Batho, The British Columbia Cancer Institute, 2656 Heather Street, Vancouver 9, BRITISH COLUMBIA
9. Dr. Gerald W. Bennett, Brookhaven National Laboratory, Upton, New York 11973
10. Dr. Martin J. Berger, Radiation Theory Section, National Bureau of Standards, Washington, D. C.
11. Dr. Hans Bichsel, Medical Radiation Physics, 3711 15th Avenue, N.E., University of Washington, Seattle, Washington 28195
12. Mr. H. Blattmann, Strahlenbiologisches Institute, University of Zurich, Zurich, SWITZERLAND
13. Dr. H. R. Blieden, National Science Foundation, 1800 G Street, N.W., Washington, D. C. 20550
14. Dr. Max L. M. Boone, Director of Radiation Oncology, Arizona Medical Center, Department of Radiology, University of Arizona, Tuscon, Arizona 85724
15. Dr. Douglas Boyd, W. W. Hansen Laboratory of Physics, Stanford University, Stanford, California 94305
16. Dr. J. J. Broerse, Radiobiological Institute of the Organization for Health Research TNO, 151 Lange Kleiweg, Rijswijk (Z-H), THE NETHERLANDS
17. Dr. L. Cabeza, Strahlenbiologisches Institut, University of Zurich, Zurich, SWITZERLAND
18. Dr. Randall S. Caswell, Neutron Physics Section, National Bureau of Standards, Washington, D. C. 20234
19. Dr. S. B. Curtis, Lawrence Berkeley Laboratory, Berkeley, California 94720

20-39. Mr. Gilbert B. Devey, Program Manager, National Science Foundation, 1800 G Street, N.W., Washington, D. C. 20550

40. Dr. J. F. Dicello, Group MP-3, Los Alamos Scientific Laboratory, Los Alamos, New Mexico 87544
41. Mr. Jean Dutrannois, Health Physics Division, CERN, Geneva 23, SWITZERLAND
42. Dr. Peter Fessenden, Department of Radiology, Stanford University Medical Center, Stanford, California 94305

43. Dr. H. Fritz-Niggli, Strahlenbiologisches Institut, University of Zurich, Zurich, SWITZERLAND
44. Dr. Michael Goiten, Department of Radiation Medicine, Massachusetts General Hospital, Cambridge, Massachusetts 02114
45. Dr. P. Haefeli, SIN, CH-5234, Villigen, SWITZERLAND
46. Dr. J. A. Helland, Group MP-3, Los Alamos Scientific Laboratory, P. O. Box 1663, Los Alamos, New Mexico 87544
47. Dr. R. M. Henkelman, The British Columbia Cancer Institute, 2656 Heather Street, Vancouver 9, British Columbia
48. Dr. G. H. Herling, Nuclear Structure and Reactions, Nuclear Sciences Division, Naval Research Laboratory, Washington, D. C. 20375
49. Dr. P. D. Holt, U.K. Atomic Energy Authority, Building 364, Harwell, Didcot, Birkshire, ENDLAND
50. Dr. Richard Hutson, Los Alamos Scientific Laboratory, P. O. Box 1663, Los Alamos, New Mexico 87644
51. Dr. Henry S. Kaplan, Department of Radiology, Stanford School of Medicine, Stanford, California 94305
52. Dr. C. J. Karzmark, Department of Radiology, Stanford University Medical Center, Stanford, California 94305
53. Professor Robert Katz, Behlen Laboratory of Physics, University of Nebraska, Lincoln, Nebraska 68508
54. Dr. Nick King, Crocker Nuclear Laboratory, University of California, Davis, Davis, California 95616
55. Dr. Morton M. Kligerman, Director, Cancer Research and Treatment Center, School of Medicine, University of New Mexico, Albuquerque, New Mexico 87115
56. Dr. E. A. Knapp, M.P. Division, Los Alamos Scientific Laboratory, Los Alamos, New Mexico 87544
57. Dr. H. B. Knowles, Physics Department, Washington State University, Pullman, Washington 99163
58. Mr. A. M. Koehler, Synchrocyclotron Laboratory, Harvard University, 44 Oxford Street, Cambridge, Massachusetts 02138
59. Dr. Lawrence H. Lanzl, Argonne Cancer Research Hospital, University of Chicago, Chicago, Illinois 60637
60. Ms. Gloria C. Li, Research Physicist, High Energy Physics Laboratory, Stanford University, Stanford, California 94305
61. Dr. C. C. Lushbaugh, Oak Ridge Associated Universities, P. O. Box 117, Oak Ridge, Tennessee 37038
62. Dr. J. T. Lyman, Lawrence Berkeley Laboratory, Berkeley, California 94720
63. Dr. Richard Madey, Department of Physics, Kent State University, Kent, Ohio 44242
64. Dr. Francis J. Mahoney, Program Director for Radiation, Biology, and Physics, National Cancer Institute, Room 10-A10, Westwood Building, 5333 Westbard Avenue, Bethesda, Maryland 20014
65. Dr. J. E. McLaughlin, Director, Radiation Physics Division, Health and Safety Laboratory, U. S. Atomic Energy Commission, 376 Hudson Street, New York, New York 10014
66. Mr. Keran O'Brien, Radiation Physics Division, Health and Safety Laboratory, U. S. Atomic Energy Commission, 376 Hudson Street, New York, New York 10014

67. Mr. Mudundi R. Raju, Los Alamos Scientific Laboratory, P. O. Box 1663, Los Alamos, New Mexico 87544
68. Mr. Douglas H. Reading, Science Research Council, Rutherford Laboratory, Chilton, Didcot, Berkshire, OX11, OOX, ENGLAND
69. Dr. J. J. Reidy, Physics Department, University of Mississippi, University, Mississippi 38677
70. Dr. Chaim Richman, Los Alamos Scientific Laboratory, P. O. Box 1663, Los Alamos, New Mexico 87544
71. Dr. David W. O. Rogers, X-Rays and Nuclear Radiations, Division of Physics, National Research Council, Ottawa, Canada, KIA-OR6
72. Dr. Louis Rosen, Los Alamos Scientific Laboratory, P. O. Box 1663, Los Alamos, New Mexico 87544
73. Dr. M. E. Schillaci, Los Alamos Scientific Laboratory, P. O. Box 1663, Los Alamos, New Mexico 87544
74. Dr. Walter Schimmerling, Lawrence Berkeley Laboratory, Bldg. 29-315C, Berkeley, California 94720
75. Dr. Roger Schneider, Bureau of Radiological Health - DEP, 5600 Fishers Lane, Rockville, Maryland 20892
76. Dr. H. Alan Schwettman, W. W. Hansen Laboratories of Physics, Stanford University, Stanford, California 94305
77. Dr. S. C. Sharma, Bethlen Laboratory of Physics, The University of Nebraska, Lincoln, Nebraska 68508
78. Dr. Yaakov Shima, SOREQ Nuclear Research Center, Yvena, ISRAEL
79. Dr. Carl R. Shonk, School of Medicine, University of New Mexico, P. O. Box 283, 915 Stanford Street, N.E., Albuquerque, New Mexico 87106
70. Dr. G. R. Stevenson, CERN-II, Geneva 23, SWITZERLAND
81. Dr. Peter Stiller, IKE, D-7 Stuttgart 80, Pfaffenwaldring 31, GERMANY
82. Dr. A. H. Sullivan, Health Physics Division, CERN, Geneva 23, SWITZERLAND
83. Dr. Richard Theus, U. S. Naval Research Laboratory, Washington, D. C. 20390
84. Dr. Ralph H. Thomas, Health Physics Division, Lawrence Berkeley Laboratory, Berkeley, California 94720
85. Dr. Georg Tisljar, Institute fur Medizin, Kernforschungsanlage, Julich, GERMANY
86. Dr. C. A. Tobias, Biology and Medicine Division, Lawrence Berkeley Laboratory, Berkeley, California 94720
87. Dr. Paul Todd, Biophysics Department, Pennsylvania State University, University Park, Pennsylvania 16802
88. Dr. W. Turkinetz, Laboratory for Nuclear Science, Massachusetts Institute of Technology, Cambridge, Massachusetts 02139
89. Dr. R. Vasudewan, Department of Electrical Engineering, University of Southern California, University Park, Los Angeles, California 90007
90. Dr. George L. Voelz, Los Alamos Scientific Laboratory, P. O. Box 1663, Los Alamos, New Mexico 87544
91. Dr. A. L. Wiley, Radiology Department, University Hospitals, The University of Wisconsin, Madison, Wisconsin 53706

92. Dr. R. W. Wood, Chief, Physics and Instrumentation Branch, Division of Biomedical and Environmental Research, U. S. Atomic Energy Commission, Washington, D. C. 20546
93. Dr. Peter Wootton, Medical Radiation Physics, 3711 15th Avenue, N.E., University of Washington, Seattle, Washington 98194